

POLITECNICO DI TORINO

Master's Degree in Aerospace Engineering



Master's Degree Thesis

Development of numerical tools for the analysis of near-field acoustic data

Supervisors

Prof. Miguel Alfonso MENDEZ

Prof. Sandra PIERACCINI

Prof. Christophe SCHRAM

Candidate

Leonardo CONTI

July 2021

Abstract

This aeroacoustics research focuses on sound-field generated by a supersonic Mach 3 jet.

The work is based on a high-speed schlieren dataset provided by the Applied Research Lab at Austin focused on the hydrodynamics field and acoustic near-field of a Mach 3 turbulent circular jet.

Mach waves are responsible for one of the most annoying noise components of a jet: crackle noise. This particular kind of noise is generated by the steepening of Mach waves which may come close to a saw-tooth-like structure characterized by sharp compressions followed by gradual expansions.

Two Data-Driven Modal Analysis techniques have been applied to this dataset, Proper Orthogonal Decomposition and multi-scale Proper Orthogonal Decomposition, to characterize the density near-field and explore in particular the occurrence of non-linear acoustic propagation effects responsible for wave steepening and eventually crackle noise.

The POD modes show wavy patterns, and the study of the main wave features like propagation path, and traveling speed allows us to identify them as Mach waves: they occur when turbulent structures inside the inner layer of the jet travel with a supersonic convective speed, and travel along a 45° inclined propagation path at speed of sound.

Non-linear propagation effects have been also investigated through the skewness statistical indicator. The results do not provide evidence of steepened wavefronts in the narrow area that has been analyzed. The study should be conducted over a wider observation area and with varying analysis parameters in the future.

Acknowledgements

Firstly, I would like to thank my supervisors: Miguel Alfonso Mendez (VKI), Sandra Pieraccini (PoliTo), and Christophe Schram (VKI). This thesis would not have been possible without their availability, commitment, patience, and guidance sharing with me their knowledge.

Then, I have to thank my family who has always supported me during these years economically and emotionally in easy times and hard times.

Last but not least, I want to thank all my friends, both university ones and home ones, who have always been on my side and made these years amazing.

Table of Contents

List of Tables	IV
List of Figures	V
Acronyms	VII
1 Physics of supersonic jet noise	1
1.1 Aims of the current study	1
1.2 Supersonic jet structure overview	1
1.3 Supersonic jet noise overview	2
1.4 Mathematical tool	4
2 Presentation of high-speed schlieren dataset	5
2.1 Technique presentation	5
2.2 Dataset details	6
2.3 Computing software and programming language	8
3 Data-Driven Modal Analysis of high-speed schlieren dataset	9
3.1 Data-Driven Modal Analysis	9
3.2 Proper Orthogonal Decomposition (POD)	12
3.2.1 Computational trick	14
3.3 Multi-scale Proper Orthogonal Decomposition (mPOD)	15
3.3.1 First constraint	16
3.3.2 Second constraint	17
4 Processing results	19
4.1 Study area selection	19
4.2 Proper Orthogonal Decomposition (POD)	20
4.2.1 Spatial structures and frequency spectra	22
4.2.2 Wave inclination angle	25
4.2.3 Waveform	27

4.2.4	Wave traveling speed	30
4.2.5	Wavelength	31
4.2.6	Mach waves	32
4.2.7	Axial origin coordinate	32
4.2.8	Skewness statistical indicator	37
4.3	Multi-scale Proper Orthogonal Decomposition (mPOD)	39
4.3.1	Spatial structures and frequency spectra	43
4.3.2	Waveform	46
5	Conclusions	50
5.1	Recap of main results	50
5.2	Open questions	51
A	2-D Fast Fourier Transform	52
B	Auto-correlation	54
C	Skewness	56
	Bibliography	58

List of Tables

4.1	Crop	20
4.2	Convention POD	22
4.3	Wave inclination angle computer	26
4.4	Wave traveling speed computed	30
4.5	Wave traveling speed error percentage	31
4.6	Wavelength	32
4.7	x/D origin	37
4.8	Skewness value	38
4.9	mPOD transfer function filters from POD modes 9,10	41
4.10	Convention mPOD	43
4.11	Extraction line starting position	49

List of Figures

1.1	Turbulent supersonic jet structure	2
1.2	Jet noise	3
2.1	Schlieren imaging technique	5
2.2	List of databases	6
2.3	Database J	6
2.4	Video frame	7
4.1	Crop	20
4.2	Mean	20
4.3	σ decay with POD	21
4.4	σ decay with DFT	21
4.5	POD modes 1,2: spatial structures and frequency spectra	22
4.6	POD modes 3,4: spatial structures and frequency spectra	23
4.7	POD modes 5,6: spatial structures and frequency spectra	23
4.8	POD modes 7,8: spatial structures and frequency spectra	23
4.9	POD modes 9,10: spatial structures and frequency spectra	24
4.10	Frequency cascade	25
4.11	Wave inclination angle computed	26
4.12	Waveform modes 1,2 POD	27
4.13	Waveform modes 3,4 POD	27
4.14	Waveform modes 5,6 POD	28
4.15	Waveform modes 7,8 POD	28
4.16	Waveform modes 9,10 POD	29
4.17	Wave traveling speed computed	31
4.18	Horizontal profile extraction modes 1,2 POD	33
4.19	Horizontal profile extraction modes 3,4 POD	33
4.20	Horizontal profile extraction modes 5,6 POD	34
4.21	Horizontal profile extraction modes 7,8 POD	34
4.22	Horizontal profile extraction modes 9,10 POD	35

4.23	POD modes superposition: first 10 modes (top-left), first 100 modes (top-right) and first 1000 modes (bottom-left), original signal (bottom-right)	35
4.24	x/D origin referred to boundary layer scheme	36
4.25	x/D origin coordinate	38
4.26	Skewness trend	39
4.27	Frequency spectrum temporal correlation matrix	40
4.28	Frequency splitting vector from POD modes 9,10	40
4.29	\widehat{K} frequency splitting vector from POD modes 9,10	41
4.30	\widehat{K} diagonal frequency splitting vector from POD modes 9,10	42
4.31	σ decay mPOD	42
4.32	mPOD modes 1,2: spatial structures and frequency spectra	43
4.33	mPOD modes 3,4: spatial structures and frequency spectra	44
4.34	mPOD modes 5,6: spatial structures and frequency spectra	44
4.35	mPOD modes 7,8: spatial structures and frequency spectra	44
4.36	mPOD modes 9,10: spatial structures and frequency spectra	45
4.37	Waveform modes 1,2 mPOD	46
4.38	Waveform modes 3,4 mPOD	47
4.39	Waveform modes 5,6 mPOD	47
4.40	Waveform modes 7,8 mPOD	48
4.41	Waveform modes 9,10 mPOD	48
A.1	2-D FFT spatial structure and frequency spectrum	52
B.1	Auto-correlation	54
C.1	Skewness working	56

Acronyms

BBSN

Broad-Band Shock associated Noise

DFT

Discrete Fourier Transform

DMD

Dynamic Modes Decomposition

FFT

Fast Fourier Transform

FSS

Fine Scale Structures

IDE

Integrated Development Environment

LSS

Large Scale Structures

mPOD

multi-scale Proper Orthogonal Decomposition

NPR

Nozzle Pressure Ratio

POD

Proper Orthogonal Decomposition

SDA

Shock Detection Algorithm

SVD

Single Value Decomposition

Chapter 1

Physics of supersonic jet noise

1.1 Aims of the current study

This thesis will apply Data-Driven Modal Analysis, a mathematical tool useful in the analysis of databases, to a high-speed dataset of frames detected through the schlieren imaging technique of a Mach 3 jet.

The following target will be of interest:

- Recognize a pattern of known features, like Mach waves; this would be a great achievement able to validate the proper working of the mathematical tool.
- Detect steepening and, if present, identify which modes are more responsible for it.
- Discover some of the main properties of the waveforms extracted along with modes propagation path.

1.2 Supersonic jet structure overview

A supersonic jet is an airflow coming out of a nozzle with an axial speed that is higher than the sound speed ($M > 1$), see Figure 1.1.

In the jet structure the following elements are present:

- Potential core (A): it is the initial part of the jet and has a conical shape starting from the exit section up to a certain number of diameters. It is characterized by a stationary, irrotational, and inviscid flow. In this region, the velocity field is uniform, steady, and equals to the nozzle exit speed.

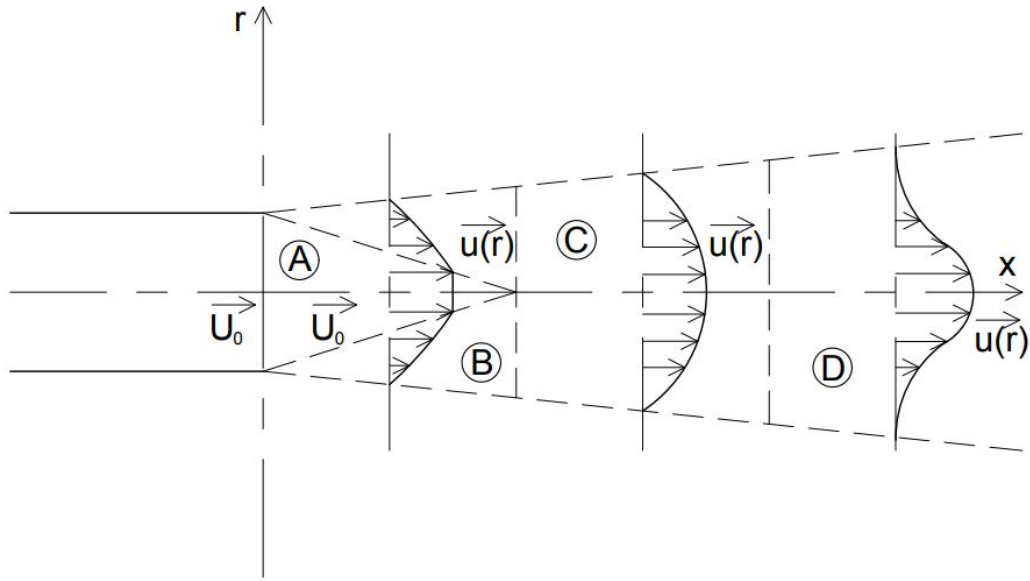


Figure 1.1: Turbulent supersonic jet structure

- Mixing region (B): it surrounds the potential core and works as a connector between that and the outside flow thanks to the viscosity. By increasing the axial coordinate, the size of this region increases at the expense of the potential core until it ends.
- Transition region (C): as the name suggests it is a transition area that is responsible for connecting the mixing region and self-similar region.
- Self-similar region (D): it is the farthest region of the jet, here velocity profiles follow a Gaussian distribution where σ represents the standard deviation.

$$u(x, r) = u_{axial}(x) \cdot e^{-\frac{r^2}{2\sigma^2}}$$

This region owes its name to the overlapping of properly non-dimensional velocity profiles.

1.3 Supersonic jet noise overview

During the last decade, the sound field generated by a supersonic jet has been one of the more interesting aeroacoustics topics. Within the noise generated under these circumstances different mechanisms of sound generation can be identified [1], see Figure 1.2:

- Shock-related noise: Broad-Band Shock associated Noise (BBSN), jet screech, and transonic resonance.
- Turbulence mixing noise: Large Scale Structures (LSS) and Fine Scale Structures (FSS).

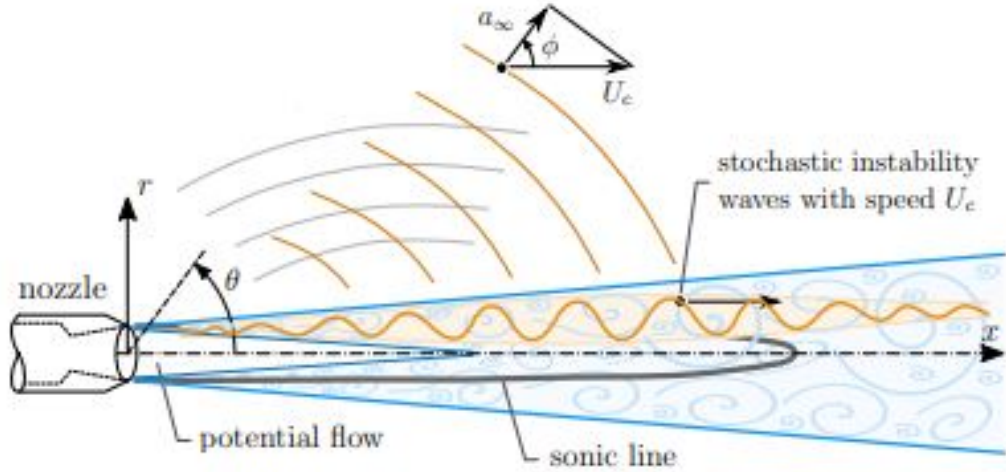


Figure 1.2: Jet noise

This analysis will focus on the last kind of noise, as suggested by the name, it occurs when turbulent structures inside the inner layer of the jet travel with a supersonic convective speed: under these circumstances, Mach waves are emitted.

Mach waves are responsible for the most annoying noise, the so-called crackle, whose pressure profile has a saw-tooth-like structure, recognizable by a sharp compression followed by a gradual expansion: this phenomenon is known as waves steepening.

The main issue during the study of crackle is perception, so it becomes necessary to implement specific algorithms, like Shock Detection Algorithm (SDA) [2], to obtain a reliable method to identify that particular noise. While Goldberg number, a non-dimensional parameter defined as the ratio of absorption length to shock formation distance, quantify how strong are cumulative non-linear distortions and viscous absorption effects:

$$\Lambda = \frac{l_\alpha}{\bar{x}}$$

- $\Lambda \gg 1$ Mach waves steepen and the onset of crackle noise is favored.

- $\Lambda \leq 1$ Mach waves vanish and the onset of crackle noise is denied.

The mechanisms which originate crackle noise are still under study, but some results have already been obtained:

- Supersonic air pockets escape from the inner layer of the jet. Along the propagation path, these blows accumulate and, thanks to cumulative non-linearities [3], end up creating the typical saw-tooth structures of crackle.
- Mach waves coalescence mechanisms. Waves propagation go through dynamics [4] revealed to be quite similar to those which take place into the oceans that may lead to non-linearities sometimes to amplification and sometimes to a reduction.
- In heated jet flows [5], an additional dynamic can bring the Mach waves to a saw-tooth-like structure: cold air micro-explosions.
- Distortion may also have a role in the process that carries the Mach waves to steepen: the actual existence of this link and the way it would work are nowadays under investigation.

1.4 Mathematical tool

Now that the problem is set, we can introduce the main character of the survey, what we are searching for should be a mathematical tool able to understand different contributes from the dataset and to choose which ones are important and which ones are negligible: the Data-Driven Modal Analysis.

A brilliant example about how modes decomposition help in studying waveform is given by [6], where an azimuthal modes decomposition reveals how the classical structure of sharp compressions and gradual expansions is not characteristic of any single mode but is a feature of their superposition.

A work based on very similar instruments to those that we will use, even more than the previous one, is [7]. There the dataset was obtained with schlieren imaging technique and the modes decomposition is a POD.

The main difference between the treatment that will be carried out and the other cited works is the portion of the sound field analyzed: while most works mainly focus on acoustic far-field and the evolution from acoustic near-field to acoustic far-field, we will study the hydrodynamic field and acoustic near-field.

Chapter 2

Presentation of high-speed schlieren dataset

2.1 Tecnique presentation

The main elements on which the optics of the schlieren imaging technique is based are resumed in the list below.

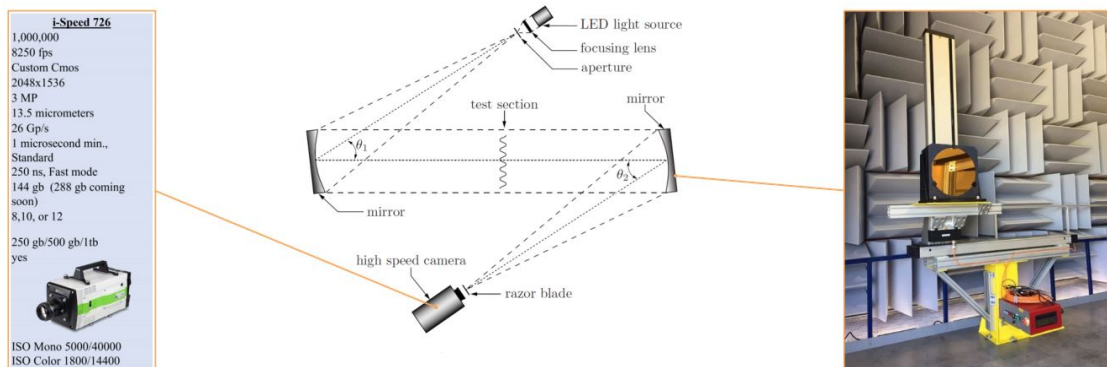


Figure 2.1: Schlieren imaging technique

- A light source: LUMINUS CBT-120 Green 510-540 nm LED operating continuously at 4,5 V and 8 A.
- A focusing lens: Nikon 28 mm, 1:2,8
- A pair of gold-coated parabolic mirrors: 12,5-inch diameter with 100-inch focal lengths

- A zoom lens: Nikon 36-72 mm, 1:3,5
- A digital camera: i-SPEED monochromatic camera manufactured by ix-Cameras, a maximum resolution of 2048 x 1536 square pixels that are 13,5 μm length with 12-bit depth

Firstly, light rays are focused into a circular aperture using the focusing lens which then illuminates the parabolic mirrors which are secured to adjustable mirror-mounts (Edmund Optics model) to allow pitch and roll fine-tuning. Then, each mirror-mount is fastened to a dedicated pair of linear translation stages that are bolted to custom-built steel frames for added mass. To achieve schlieren images, a razor blade cut-off is inserted to block portions of the light entering the digital camera. Lastly, the zoom lens allows to obtain large fields of view and the digital camera allows to acquire the schlieren images. Note that the razor blade and optics are aligned to accommodate a 45° cut-off angle, a 50% cut-off as opposed to a 0° or to a 90° cut-off which is commonly performed. The scheme in Figure 2.1 describes the optics of the Z-type schlieren diagram.

2.2 Dataset details

Database identifier	frame rate (x 1000)	Field of View	NPR	# images (x 100)	Shutter (ms)cutoff angle	pixel resolution	Calibration images?	file name	notes	
A	50	large fow with nozzle and flow	26	12k	x	45	672 x 456	No	E:\Mach3\50k\NPR26_Nozzle_Exit\Mach3_npr26_50k	
B	50	large fow with nozzle and flow	37	10k	x	45	672 x 456	No	E:\Mach3\50k\NPR37_Nozzle_Exit\Mach3_npr37_50k	
C	100	nozzle exit region	20			45	840 x 216	Yes	E:\Mach3\100k\NPR20_Nozzle_Exit\Mach3_NPR20_100k	
D	100	post potential core (x = 170, y = 0)	20			45	840 x 216	Yes	E:\Mach3\100k\NPR20_X17_Y0\Mach3_NPR37_100k_X17_Y0	
E	100	post potential core (x = 170, y = 3D)	20			45	840 x 216	Yes	E:\Mach3\100k\NPR20_X17_Y3\Mach3_NPR37_100k_X17_Y3	
F	100	nozzle exit region	37			45	840 x 216	Yes	E:\Mach3\100k\NPR37_Nozzle_Exit\Mach3_NPR37_100k	calibration images include background and ruler
G	100	post potential core (x = 170, y = 0)	37			45	840 x 216	Yes	E:\Mach3\100k\NPR37_X17_Y0\Mach3_NPR37_100k_X17_Y0	calibration images include background and ruler
H	100	post potential core (x = 170, y = 3D)	37			45	840 x 216	Yes	E:\Mach3\100k\NPR37_X17_Y3\Mach3_NPR37_100k_X17_Y3	
I	150	nozzle exit region	37			45	672 x 132	No	E:\Mach3\150k\NPR37_Nozzle_Exit\Mach3_npr37_150k	
J	200	nozzle exit region	20			45	840 x 96	Yes	E:\Mach3\200k\NPR20_Nozzle_Exit\Mach3_NPR20_200k	
K	200	nozzle exit region	20			45	672 x 96	No	E:\Mach3\200k\Noncalibrated\NPR20_nozzle_exit\Mach3_npr20_200k	
L	200	nozzle exit region	37			45	840 x 96	Yes	E:\Mach3\200k\NPR37_Nozzle_Exit\Mach3_NPR37_200k	
M	200	nozzle exit region	37			45	672 x 96	No	E:\Mach3\200k\Noncalibrated\NPR37_nozzle_exit\Mach3_npr37_200k	
N	200	nozzle exit region	37			45	672 x 96	No	E:\Mach3\200k\Reflection\Mach3_reflection_200k	jet flow parallel to large flat, acoustically reflective plate

Database identifier	frame rate (x 1000)	Field of View	NPR	# images (x 100)	Shutter (ms)cutoff angle	pixel resolution	Calibration images?	file name	notes	
1	500	y = 2.50, x = 8D-20D	37	16.384	1	45	672 x 24	Yes	E:\Mach3_Coalescence_Nozzle2019\test1_50005	y-location denotes centerline of image
2	500	y = 2.50, x = 8D-20D	37	16.384	2	45	672 x 24	Yes	E:\Mach3_Coalescence_Nozzle2019\test2_50006	▲x = 2 inches
3	500	y = 2.50, x = 2D-14D	37	16.384	2	45	672 x 24	Yes	E:\Mach3_Coalescence_Nozzle2019\test3_50011	
4	50	y = 2.50, x = 2D-14D	37	16.384	20	45	672 x 456	Yes	E:\Mach3_Coalescence_Nozzle2019\test4_50014	
5	300	y = 4D, x = 2D-14D	37	16.384	1usec	45	620 x 66	Yes	E:\Mach3_Coalescence_Nozzle2019\test5_50023 (24)	dots in images; data broken up in two sets
6	300	y = 4D, x = 10D-22D	37	16.384	1usec	45	620 x 66	Yes	E:\Mach3_Coalescence_Nozzle2019\test6_50028	
7	300	y = 4D, x = 18D-30D	37	16.384	1usec	45	620 x 66	Yes	E:\Mach3_Coalescence_Nozzle2019\test7_50032	
8	300	first dot +4x, 1y(dots are v2 apart)	37	16.384	1usec	45	620 x 66	Yes	E:\Mach3_Coalescence_Nozzle2019\test8_50036	camera at 45 degree angle

Figure 2.2: List of databases



Figure 2.3: Database J

The Overview of Mach 3 Nozzle Databases [8] contains the list of files in Figure 2.2 for a gas whose theoretical properties are:

- Nozzle Pressure Ratio, $\text{NPR} = 36,73$
- Total temperature, $T_0 = 241 \text{ K}$
- Static temperature, $T_s = 104 \text{ K}$
- Jet speed, $U = 613 \text{ m/s}$
- Reynolds number, $\text{Re} = 7,4 \times 10^6$

The focus of this analysis will be on a sequence of 10001 frames from the dataset J, highlighted in Figure 2.3, which is characterized by:

- $\text{NPR} = 20$
- Image dimensions (format “length x height” in pixels) = 840×96
- Sampling frequency, $f = 2 \times 10^5 \text{ Hz}$.

We recreate an x1000 slow-motion from the dataset J by cropping the useful part of every single frame. In Figure 2.4 a frame of this video is reported.

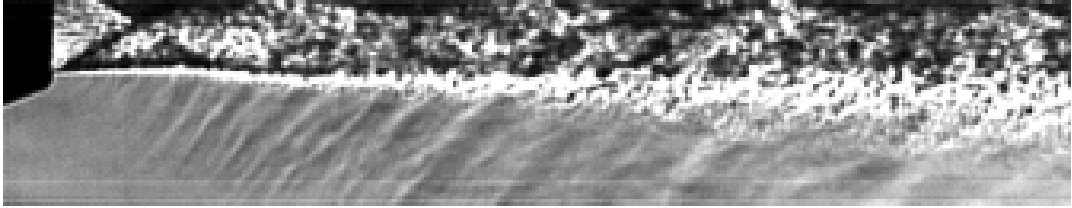


Figure 2.4: Video frame

The choice fell on slow-motion because using the original sampling frequency the video would have last only 0,05 seconds, clearly not enough to understand the propagation mechanisms involved.

A very important calibration that has to be known before proceeding is the schlieren imaging millimeter-pixel ratio. To implement it, firstly we identify the center of the jet from the background triangle and then we detect how many pixels correspond to the jet half-diameter. At this point, the known jet diameter in millimeters allows us to compute a good approximation of the wanted ratio as follows:

$$\gamma = \frac{mm}{px} = \frac{D_{j,mm}}{D_{j,px}} \approx 0,55$$

7

2.3 Computing software and programming language

Image processing will be the most important computer tool that we will apply. A very efficient programming language that fits perfectly for this purpose is Python: a high-level and object-oriented programming language.

The computing software we will rely on is Spyder: an open-source and cross-platform Integrated Development Environment (IDE) located within the distribution platform Anaconda.

Chapter 3

Data-Driven Modal Analysis of high-speed schlieren dataset

3.1 Data-Driven Modal Analysis

Data-Driven Modal Analysis is a powerful mathematical tool that is useful during the processing of big data. This methodology consists of a decomposition of the given dataset along rank 1 structures named modes, so a linear combination of these modes gives as result the original set of data. Focusing on the modes, every single one is characterized by a spatial structure and a temporal structure which are also the basis respectively for the spatial domain and the temporal domain.

The concept of Data-Driven Modal Analysis is very wide and can be applied for different tasks, here we report some of the most common ones.

- Recognize known patterns into some modes to classify them.
- Filter some negligible modes to compress the dimension of the dataset.
- Select only some important modes with the aim of model order reduction.

The time-resolved schlieren images constitute the set of data, each single image is shown into a uniform grid in the spatial domain and represents a temporal snapshot of the field. Reshaping all these snapshots into column vectors we can assemble the data matrix, where the column space is the space domain and the row space is the time domain. Moreover, the number of snapshots defines the number of columns n_t and the product of the grid dimensions n_x and n_y gives as result the number of rows n_s .

$$D = \begin{bmatrix} d_1[1] & \cdots & d_k[1] & \cdots & d_{n_t}[1] \\ \vdots & \vdots & \vdots & \vdots & \vdots \\ d_1[k] & \cdots & d_k[k] & \cdots & d_{n_t}[k] \\ \vdots & \vdots & \vdots & \vdots & \vdots \\ d_1[n_t] & \cdots & d_k[n_t] & \cdots & d_{n_t}[n_t] \end{bmatrix}$$

In the analytical formulation the dependence of the data matrix from space is shown by the position x_i , the dependence of the data matrix from time is shown by the instant t_k . Letting us R denote the rank of data matrix and M_r the r -th mode, we have:

$$D(x_i, t_k) = \sum_{r=1}^R M_r(x_i, t_k)$$

There are two different ways to read this matrix, when not indicated differently we will refer to the first one.

- 'Space view': time evolution of a space basis.
- 'Time view': spatial structure of a time basis.

Both these views lead the data matrix to a decomposition highlighted in the discrete form where we introduce: the amplitude coefficients σ_r ; the basis in space, spatial structures ϕ_r ; the basis in time, temporal structures ψ_r .

$$D[i, k] = \sum_{r=1}^R M_r[i, k] = \sum_{r=1}^R \sigma_r \phi_r[i] \psi_r[k]$$

The only precaution in this kind of formulation is that both the norm of the spatial structures and the norm of the temporal structures are equal to 1, so the amplitude coefficients represent the energy of the modes. Using a compact matrix notation, where the apex 'T' is used for transposition, the data matrix becomes:

$$D = \Phi \Sigma \Psi^T$$

Where:

$$\Phi = \begin{bmatrix} \phi_1[i] & \cdots & \phi_R[i] \\ \vdots & \vdots & \vdots \end{bmatrix}$$

$$\Sigma = \begin{bmatrix} \sigma_1 & 0 & 0 \\ 0 & \ddots & 0 \\ 0 & 0 & \sigma_R \end{bmatrix}$$

$$\Psi = \begin{bmatrix} \psi_1[k] & \cdots & \psi_R[k] \\ \vdots & \vdots & \vdots \end{bmatrix}$$

Namely, $\Phi \in \mathbb{R}^{n_s \times n_t}$ is a matrix that contains the space basis as its columns, $\Sigma \in \mathbb{R}^{n_t}$ is a diagonal matrix that contains the amplitudes as its diagonal and $\Psi \in \mathbb{R}^{n_t \times n_t}$ is a matrix that contains the time basis as its columns.

This equation named also Generalized Factorization, is the key algorithm of Modal Analysis which allows computing the spatial structures once the temporal structures are given and, vice versa, to compute the temporal structures once the spatial structures are given, because Σ is a diagonal matrix, and both the columns of Φ and the columns of Ψ are normalized, so it is not possible to choose this last two matrices simultaneously. The summary below shows how this process works.

- 'Space view': time evolution of a space basis.

$$\Psi \rightarrow D(\Psi^T)^{-1} = \Phi \Sigma = C \rightarrow \|C_r\| = \|\phi_r \sigma_r\| \rightarrow \Phi = D(\Psi^T)^{-1} \Sigma^{-1}$$

- 'Time view': the spatial structure of a time basis.

$$\Phi \rightarrow \Phi^{-1} D = \Sigma \Psi^{-1} = C \rightarrow \|C_r\| = \|\psi_r \sigma_r\| \rightarrow \Psi = (\Sigma^{-1} \Phi^{-1} D)^T$$

In the above formulations, the apex '-1' denotes matrix inversion. Another important observation is that if the number of modes is lower than the rank R of the data matrix we are working with an approximation of the dataset called Reduced Model Order or Filtered Data.

$$\widetilde{D} = \widetilde{\Phi}_P \widetilde{\Sigma}_P \widetilde{\Psi}_P^\dagger$$

In the equation above, the 'tilde' is used for matrix approximation and the apex 'dagger' denotes transposed and conjugated matrix. There are two kinds of Modal Analysis and, in this work, we will focus mainly on the last one.

- Frequency-based, like Discrete Fourier Transform (DFT) or Dynamic Modes Decomposition (DMD). The advantage of these methods is the possibility to operate spectral separation and represent the spatial structure of each frequency distinguishing it from the others; on the other hand, the disadvantages are the absence of time localization and the poor convergence and poor conditioning of the algorithms.
- Energy-based, like Proper Orthogonal Decomposition (POD). The advantages of this method are the energy optimality, which gives the best approximation

for the chosen rank, and the robustness of the algorithm; on the other hand, the disadvantage is the risk of spectral mixing, because more frequencies are involved in the representation of every single spatial structure.

3.2 Proper Orthogonal Decomposition (POD)

Moving deeper into Proper Orthogonal Decomposition there are two ways to implement energy optimality criteria:

- Minimize the error as Euclidean norm of the difference between the original data matrix and its approximation:

$$\min \left(\| D - \widetilde{D} \| \right) = \min \left(\| D - D(\psi_r \psi_r^\dagger) \|_2 \right)$$

- Maximize the variance as Euclidean norm of the amplitudes:

$$\max \left(\sigma_r \right) = \max \left(\| \phi_r \sigma_r \|_2 \right) = \max \left(\| D \phi_r \|_2 \right)$$

At this point, it is necessary to introduce an auxiliary function A defined as:

$$A = f(x, y) + \lambda g(x, y) = \left\{ (D\psi)^\dagger (D\psi) \right\} + \lambda \{ 1 - \psi^\dagger \psi \}$$

Where $f(x, y)$ and $g(x, y)$ are function of space, and λ is a Lagrange multiplier. This mathematical method allow to localize local maxima and local minima of a function $f(x, y)$ by adding the product between a function $g(x, y) = 0$ and a Lagrange multiplier λ . More information about it can be found in [9].

The orthonormality of the time basis, i.e. the outer product of the time basis is equal to 1, allows us to respect the constraint that the space function $g(x, y)$ is equal to 0.:

$$\langle \psi, \psi \rangle = \psi^\dagger \psi = 1$$

Through an easy formulation, the auxiliary function can be written as:

$$A = \left\{ (D\psi)^\dagger (D\psi) \right\} + \lambda \{ 1 - \psi^\dagger \psi \} = \psi^\dagger (D^\dagger D) \psi + \lambda - \lambda \psi^\dagger \psi$$

Now, imposing that the derivative of the auxiliary function with respect to the time basis is equal to 0, transform the equation in an eigenvalues and eigenvectors problem.

$$\frac{\partial A}{\partial \psi} = (D^\dagger D) \psi - \lambda \psi = 0 \rightarrow (D^\dagger D) \psi = \lambda \psi$$

The matrix which contains the eigenvectors is defined as the product between the dagger data matrix and the data matrix. The result of this operation is also known as the temporal correlation matrix.

If we assume the data matrix to be a row vector of column vectors d containing all the values assumed at the same time in different positions:

$$D = [d_1 \quad \cdots \quad d_i \quad d_j \quad \cdots \quad d_{n_t}]$$

Then we can introduce the temporal correlation matrix:

$$K = K[i, j] = d_i^T d_j = \langle d_i, d_j \rangle = \sum_{i=1}^{n_t} d_i[i] d_j[i]$$

Whose compact form is:

$$K = D^T D = \Psi_P \Sigma_P^2 \Psi_P^T$$

The just obtained matrix K has many properties, which define POD features, that deserve to be observed in detail.

- It is a positive definite matrix: the rank of the data matrix is equal to the number of the non-zero eigenvalues of the temporal correlation matrix.
- It has only real and positive eigenvalues: the dagger matrix becomes a transposed matrix because the data matrix is real.
- It has a set of orthogonal eigenvectors: the inverse of the eigenvectors matrix is equal to its transpose, and the eigenvectors will be real because the data matrix is real.
- Since in the previous demonstration the variance of each rank approximation is maximized, the orthogonal eigenvectors of the spatial-temporal matrix produce the best possible basis in terms of energy optimality.
- The choice of the temporal structures reflects in the resulting spatial structures.

At this point, thanks to the Generalized Factorization algorithm, we can compute the time basis and the spatial structures from the temporal structures.

$$\Psi \rightarrow D(\Psi^T)^{-1} = \Phi \Sigma = C \rightarrow \|C_r\| = \|\phi_r \sigma_r\| \rightarrow \Phi = D(\Psi^T)^{-1} \Sigma^{-1}$$

Usually, the magnitude order of n_s is greater or equal than the one of n_t , so the number of rows is way larger or almost the same as the number of columns in the data matrix and the 'space view' is convenient, later another point of view will be proposed.

However, regardless of the chosen point of view, the Proper Orthogonal Decomposition, implemented in the way showed in this work, results in the Single Value Decomposition of the data matrix:

$$D = USV^T$$

We will use this kind of decomposition, where: U equals Φ ; S equals Σ ; V equals Ψ .

This is not always true because the POD is a more general concept than the SVD, but they become equal using a Cartesian space-time mesh and Eulerian inner product. This coincidence allows to extend the Single Value Decomposition properties to the Proper Orthogonal Decomposition: the most important of these is surely the Eckart Young Minsky Theorem which ensures one more time the energy optimality criteria.

3.2.1 Computational trick

There is a computational trick that becomes very useful in the rare case in which the magnitude order of n_s is smaller than the one of n_t , so the number of rows is way smaller than the number of columns in the data matrix and the 'time view' is convenient. So, thanks to the introduction of the spatial correlation matrix instead of the temporal correlation matrix, we can reduce the requirements of computational power.

If we assume the data matrix to be a column vector of row vectors d containing all the values assumed in the same position at different times:

$$D = \begin{bmatrix} d_1 \\ \vdots \\ d_i \\ d_j \\ \vdots \\ d_{n_s} \end{bmatrix}$$

This time we obtain spatial correlation matrix:

$$C = C[i, j] = d_i^T d_j = \langle d_i, d_j \rangle = \sum_{i=1}^{n_s} d_i[i] d_j[i]$$

Which in compact form becomes:

$$C = DD^T = \Phi_P \Sigma_P^2 \Phi_P^T$$

The just obtained matrix C , under these particular conditions, allows us to implement POD by saving computational power.

As seen for the temporal correlation matrix, thanks to the Generalized Factorization algorithm, we can compute the space basis and the temporal structures from the spatial structures.

$$\Phi \rightarrow \Phi^{-1}D = \Sigma\Psi^{-1} = C \rightarrow \|C_r\| = \|\psi_r\sigma_r\| \rightarrow \Psi = (\Sigma^{-1}\Phi^{-1}D)^T$$

More information about the Proper Orthogonal Decomposition can be found in [10, 11, 12, 13, 14, 15, 16, 17, 18].

3.3 Multi-scale Proper Orthogonal Decomposition (mPOD)

Another kind of Modal Analysis used in this work is the multi-scale Proper Orthogonal Decomposition (mPOD). This decomposition is a hybrid method that combines the advantages of both frequency-based decomposition (like DFT or DMD) and energy-based decomposition (like POD).

The first step is to consider the data matrix in the space-frequency domain, instead of the space-time domain. The 'hat' is used to recognize this matrix which is obtained by multiplying the data matrix by the complex conjugate of the Fourier matrix, the 'overline' denotes this operation. Here, the Fourier matrix is a complex and symmetric Vandermonde matrix.

$$\widehat{D} = D\overline{\Psi}_F$$

$$\widehat{D} = \begin{bmatrix} \widehat{d}_1[1] & \cdots & \widehat{d}_k[1] & \cdots & \widehat{d}_{n_t}[1] \\ \vdots & \vdots & \vdots & \vdots & \vdots \\ \widehat{d}_1[k] & \cdots & \widehat{d}_k[k] & \cdots & \widehat{d}_{n_t}[k] \\ \vdots & \vdots & \vdots & \vdots & \vdots \\ \widehat{d}_1[n_t] & \cdots & \widehat{d}_k[n_t] & \cdots & \widehat{d}_{n_t}[n_t] \end{bmatrix}$$

$$\Psi_F = \frac{1}{\sqrt{n_t}} \begin{bmatrix} 1 & 1 & 1 & \cdots & 1 \\ 1 & \omega & \omega^2 & \cdots & \omega^{n_t-1} \\ 1 & \omega^2 & \omega^4 & \cdots & \omega^{2(n_t-1)} \\ \vdots & \vdots & \vdots & \ddots & \vdots \\ 1 & \omega^{n_t-1} & \omega^{2(n_t-1)} & \cdots & \omega^{(n_t-1)^2} \end{bmatrix}$$

Then we have to define a matrix that contains the information about the frequency content in the data, as the temporal correlation matrix contains the information about the time localization of the events. The solution is the frequency spectrum of the temporal correlation matrix, denoted by the 'hat', which is obtained from the multiplication below.

$$\widehat{K} = \overline{\Psi}_F K \overline{\Psi}_F$$

The formulation above involves the temporal correlation matrix discussed in the previous chapter and the just-defined Fourier matrix.

The mPOD aims to isolate the contribution of different scales along the diagonal of the frequency spectra temporal correlation matrix. This task is accomplished through a decomposition that allows us to obtain energy optimality and spectral purity while keeping the stationarity assumption. To achieve this result, we add a spectral constraint to the POD energy optimality thanks to two key observations.

3.3.1 First constraint

The first observation suggests that the POD of a filtered data is constrained within the pass-band region of the filter. To demonstrate this statement, we can apply a low-pass filter to the data matrix before implementing POD. The filtered data matrix is obtained by computing the Schur product between the space-frequency domain data matrix and the low-pass filter, which is a 1-D transfer function. The Schur product is denoted by \odot and is also known as the Hadamard product; it calculates the multiplication between the elements which have the same coordinates returning a matrix with the same dimensions of the factors.

$$\widehat{D}_L = \widehat{D} \odot H'_L$$

At this point, it becomes possible to come back to the space-time domain of the low-pass filtered data matrix multiplying by the Fourier matrix as in the expression below.

$$D_L = \left[(D \overline{\Psi}_F) \odot H'_L \right] \Psi_F$$

Now, through one last step, we can compute the low-pass filtered temporal correlation matrix using its definition as in the following formulation:

$$K_L = D_L^\dagger D_L$$

$$K_L = \overline{\Psi}_F \left[(\widehat{D} \odot H'_L)^\dagger (\widehat{D} \odot H'_L) \right] \Psi_F = \overline{\Psi}_F \left[(\widehat{D}^\dagger \widehat{D}) \odot ((H'_L)^\dagger \odot H'_L) \right] \Psi_F$$

Thanks to the introduction of the cross-spectral density matrix we can conclude the treatment as follows:

$$K_F = \widehat{D}^\dagger \widehat{D} = \Psi_F [D^\dagger D] \overline{\Psi}_F$$

$$K_L = \overline{\Psi}_F [K_F \odot H_L] \Psi_F$$

Focusing more closely on the Schur product between the dagger low-pass filter and the low-pass filter, it appears how combining two 1-D transfer functions we obtain a 2-D filter. This filter allows us to extract a square from each orthant in symmetrical positions of the data matrix, so if a frequency is not contained in the filtered data matrix it will not be present in any mPOD mode.

3.3.2 Second constraint

The second observation is related to how orthogonal complements in the frequency domain lead to orthogonal complements in the correlation domain. This result is achieved by filtering the space-frequency domain data matrix with three different 1-D transfer functions: in addition to the low-pass filter introduced in the previous section, we consider also a band-pass filter and a high-pass filter.

$$\widehat{D}_L = \widehat{D} \odot H'_L$$

$$\widehat{D}_M = \widehat{D} \odot H'_M$$

$$\widehat{D}_H = \widehat{D} \odot H'_H$$

By deeply analyzing the structure of these filters it appears clear how they are complementary and orthogonal: confirmation of this statement is given by the equation below.

$$H'_L + H'_M + H'_H = 1$$

Repeating the steps followed previously, we come back to the space-time domain of the filtered data matrix, and then we compute the filtered temporal correlation matrix from its definition.

$$D = [\widehat{D} \odot (H'_L + H'_M + H'_H)] \Psi_F$$

$$K = D^\dagger D = \Psi [K_F \odot (H_p + H_m)] \overline{\Psi}_F$$

Thanks to the properties of complementarity and orthogonality it becomes possible to divide the filters into two categories:

- Pure terms: products between a dagger transfer function and the same transfer function.

$$H_p = (H'_L)^\dagger H'_L + (H'_M)^\dagger H'_M + (H'_H)^\dagger H'_H$$

- Mixed terms: products between a dagger transfer function and a different transfer function.

$$H_m = (H'_L)^\dagger H'_M + (H'_L)^\dagger H'_H + (H'_M)^\dagger H'_L + (H'_M)^\dagger H'_H + (H'_H)^\dagger H'_L + (H'_H)^\dagger H'_M$$

The pure terms completely contain the main diagonal and the main anti-diagonal, while the mixed terms fill the rest of the filtered temporal correlation matrix: the latter can be neglected to obtain an approximation considering only the pure terms.

$$K \approx K_L + K_M + K_H$$

Lastly, we can conclude that the absence of any kind of overlapping assures us that the orthogonality survives across these transformations.

More information about the multi-scale Proper Orthogonal Decomposition can be found in [19, 20, 21].

Chapter 4

Processing results

4.1 Study area selection

In this chapter, we describe the actual processing of the high-speed schlieren dataset.

Firstly we have to crop the frames to find an area where Data-Driven Modal Analysis decomposition can give valid results. We complete this task following these indications:

- Crop outside the jet boundary layer. The chaotic structures which characterize the inner part of the jet have very high energy contents and so, also a little involvement within the crop, may compromise the entire work. Studies on the subject proved how boundary layer limits respect the equation $y = 0,1x$. This law can help especially when the edge of the boundary layer is not easy to identify, but the schlieren imaging technique makes it very intuitive to recognize.
- Crop outside measurement imperfections. The dataset may present some anomalies, like the two light lines into the lower part of the images, and it is better to exclude them from the crop.

According to these indications we selected the study area surrounded by the red rectangle in Figure 4.1, and we place the origin of the axes where the red cross represents the center of the jet origin section.

Table 4.1 sums up crop dimension. Non-dimensional axial coordinates confirm how this analysis involves hydrodynamic field and acoustic near-field. The millimeter-pixel ratio gives us a physical measurement of the selected study area.

This case study is a stationary flow, so we have to remove the mean flow computed along the column of the data matrix as temporal average. The mean

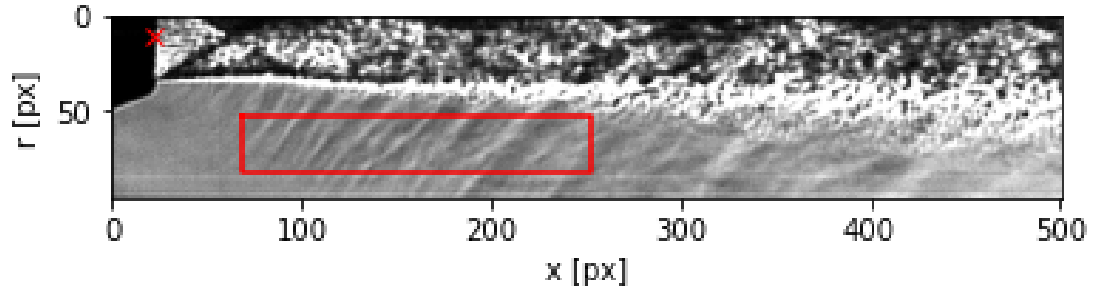


Figure 4.1: Crop

Axis	x	r
Non-dimensional coordinate [/D]	1 - 5	0,9 - 1,6
Length [px]	184	32
Length [mm]	101,2	17,6

Table 4.1: Crop

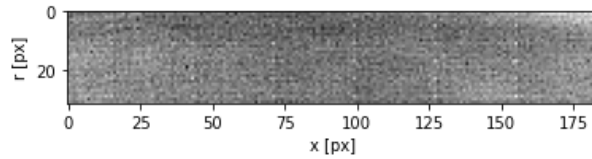


Figure 4.2: Mean

flow reconstruction is shown in Figure 4.2, then we subtracted it to the original data matrix which becomes ready to be analyzed.

4.2 Proper Orthogonal Decomposition (POD)

The Proper Orthogonal Decomposition technique, as presented in the previous chapter, brings us to 10001 modes sorted according to decreasing energy.

A first way to visualize the results of this decomposition is to plot the σ decay, see Figure 4.3. This plot shows the amplitudes of every single mode along the y-axis and the number of the modes along the x-axis. Figure 4.4 shows the σ decay of DFT, a frequency-based decomposition. The x-axis is represented in a logarithmic scale to focus the attention on the more energetic modes.

The comparison between these decays allows us to comment on the main reasons that led us to use POD:

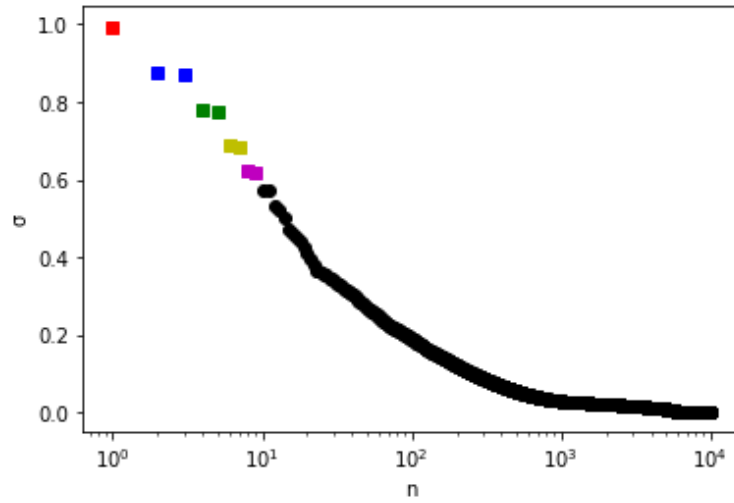


Figure 4.3: σ decay with POD

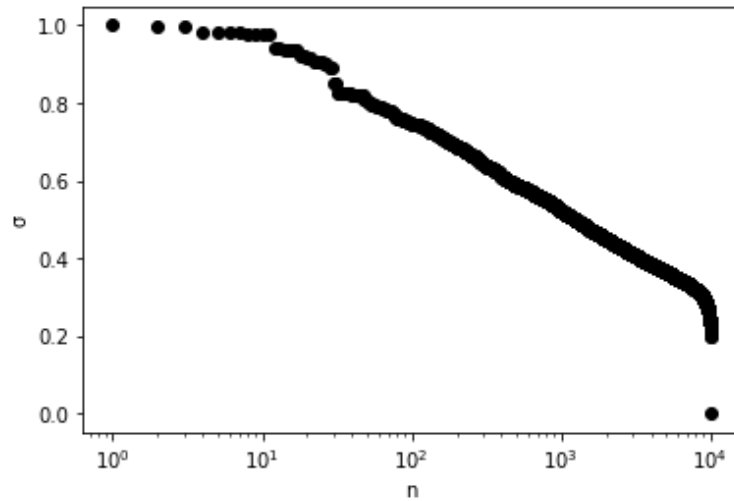


Figure 4.4: σ decay with DFT

- POD σ decay is faster, so a single pair of modes shows the information contained in much more DFT modes, and the modes coupling is real within the dataset.
- DFT σ decay is more gentle, so more modes are required to show the information contained in a single pair of POD modes; furthermore, the modes coupling depends on the decomposition itself.

It is worth noting that POD modes are coupled: first with second, third with

fourth, fifth with sixth, and so on. Deeply observing:

- σ of the modes which compose a pair is similar;
- σ of the modes within a couple is well distinct from that of nearby couples;
- increasing mode number σ get closer.

Pair	Modes	Color
1	1,2	Red
2	3,4	Blue
3	5,6	Green
4	7,8	Yellow
5	9,10	Magenta
Sum	1,2,...,n	Cyan

Table 4.2: Convention POD

During this analysis, we will use a convention to focus on the first 10 modes, highlighted in Table 4.2, which recap the composition of every couple of modes and associate them a color. The last line of Table 4.2 refers to the reconstruction of structures obtained summing modes from 1 to an arbitrary value n .

4.2.1 Spatial structures and frequency spectra

The firsts POD results that we are going to analyze are the spatial structures and the frequency spectra.

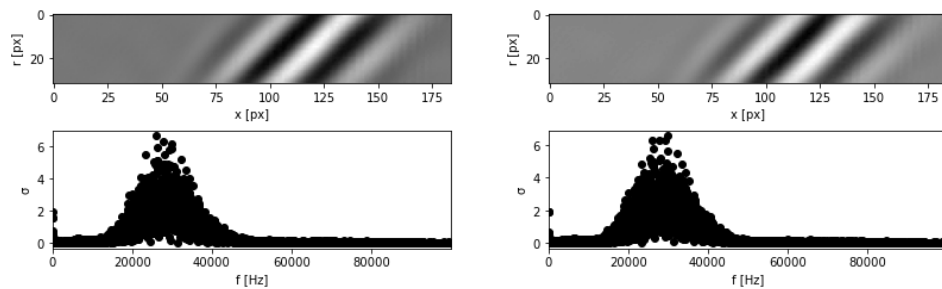


Figure 4.5: POD modes 1,2: spatial structures and frequency spectra

Spatial structures correspond to the matrix Φ (see chapter 3), reshaped from column arrays into $n_x \times n_y$ matrices. Frequency spectra represent σ amplitudes

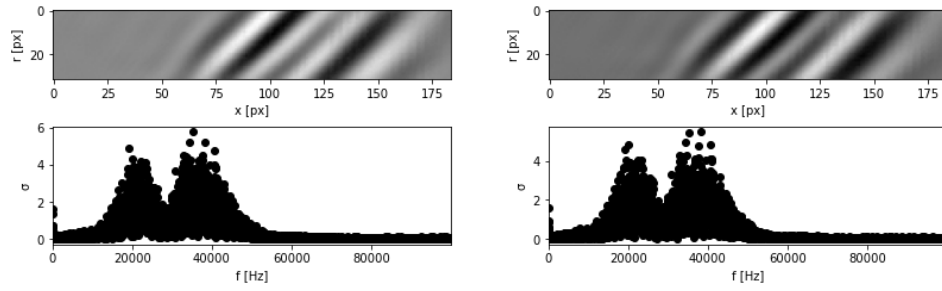


Figure 4.6: POD modes 3,4: spatial structures and frequency spectra

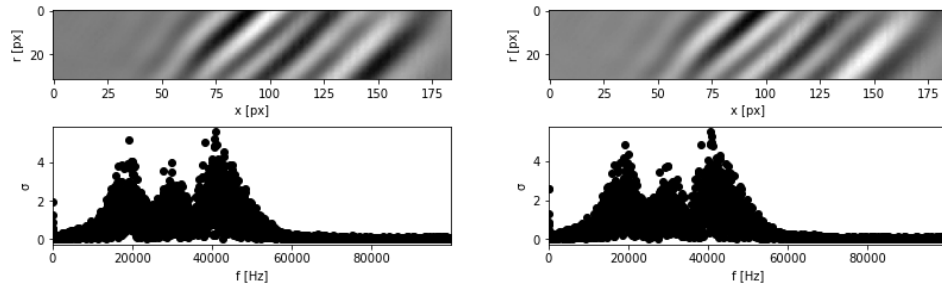


Figure 4.7: POD modes 5,6: spatial structures and frequency spectra

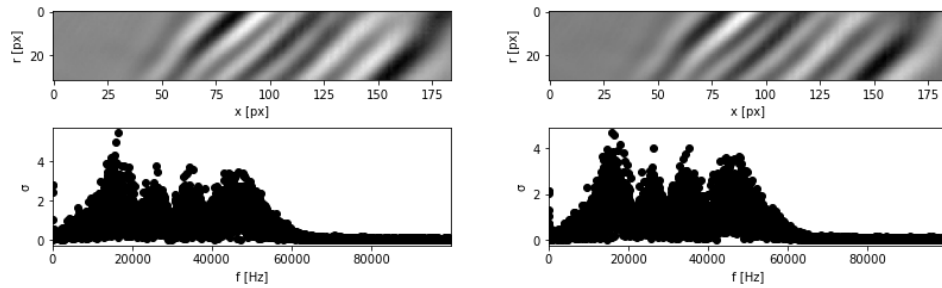


Figure 4.8: POD modes 7,8: spatial structures and frequency spectra

associated with frequencies. Bearing in mind that we want to highlight the relationship between the two modes which form a pair, we can make some observations in detail case by case:

- POD modes 1,2 (Figure 4.5):

Spatial structures reveal waves insurgency from a certain coordinate, they appear as almost regular and they show a certain inclination.

Frequency spectra are characterized by a single peak at a value equals to 28

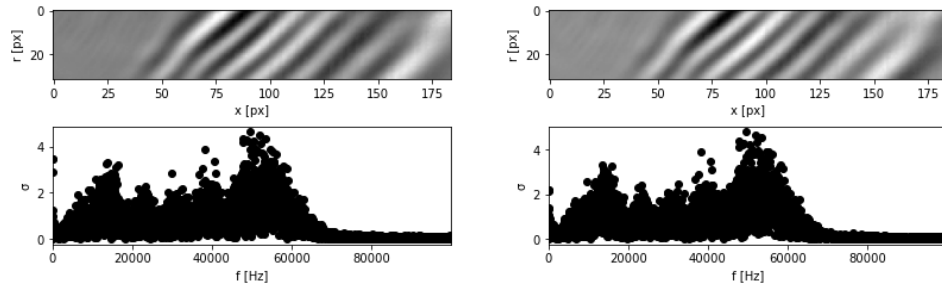


Figure 4.9: POD modes 9,10: spatial structures and frequency spectra

kHz.

- POD modes 3,4 (Figure 4.6):
Spatial structures reveal waves insurgency from a certain coordinate, they appear a bit less regular and present more oscillations than the first pair and they show a certain inclination.
Frequency spectra are characterized by two peaks at values equal to 21 kHz and 37 kHz.
- POD modes 5,6 (Figure 4.7):
Spatial structures reveal waves insurgency from a certain coordinate, they appear a bit less regular and present more oscillations than the previous pairs and they show a certain inclination.
Frequency spectra are characterized by three peaks at values equal to 19 kHz, 30 kHz, and 41 kHz.
- POD modes 7,8 (Figure 4.8):
Spatial structures reveal waves insurgency from a certain coordinate, they appear a bit less regular and present more oscillations than the previous pairs and they show a certain inclination.
Frequency spectra are characterized by four peaks at values equal to 16 kHz, 26 kHz, 35 kHz, and 46 kHz.
- POD modes 9,10 (Figure 4.9):
Spatial structures reveal waves insurgency from a certain coordinate, they appear a bit less regular and present more oscillations than the previous pairs and they show a certain inclination.
Frequency spectra are characterized by five peaks at values equal to 14 kHz, 23 kHz, 31 kHz, 39 kHz, and 51 kHz.

Summarizing, the spatial structures which compose every single pair of modes are complementary. By considering two modes at a time, we can make reconstructions that simulate waves motion through Generalized Factorization (see chapter 3). This process can be seen as model order reduction which is one of the aims for which Data-Driven Modal Analysis has been developed.

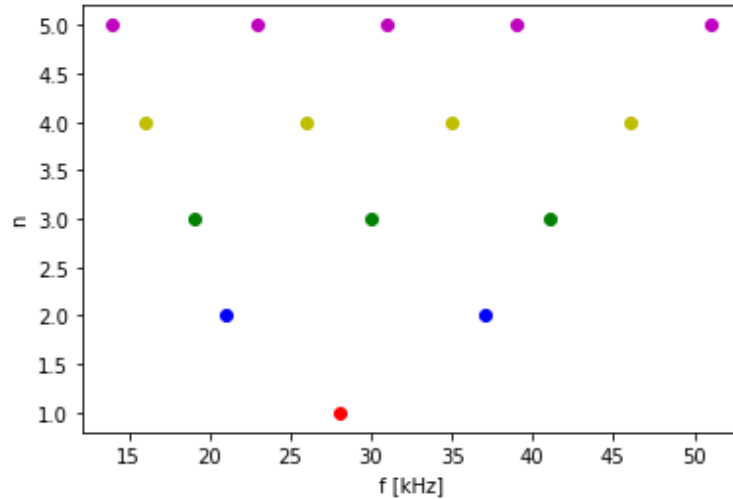


Figure 4.10: Frequency cascade

Regarding frequency spectra, we noticed that the first pair of modes has a single peak, the second pair has two peaks, the third pair has three peaks, and so on. By analyzing their location within Figure 4.10 we discover a "frequency cascade" where, moving from the most energetic pair to the least energetic pair, every group of n peaks is divided into a wider, lower group of $n+1$ peaks.

4.2.2 Wave inclination angle

We can see how modes contain waves that travel with a certain inclination and one of the first tasks will be to identify these angles and to check if their values equal some known values: this could be a very important first step for identifying the waves.

The mathematical tool that we choose to compute wave inclination angle is 2-D Fast Fourier Transform (FFT) presented in Appendix A.

In summary, we compute these angles as the arctangent of the ratio between the wavenumber who match the peak of the function along the axial coordinate $k_{x_{max}}$ and wavenumber who match the peak of the function along the radial coordinate $k_{y_{max}}$:

$$\theta = \arctan\left(\frac{k_{x_{max}}}{k_{y_{max}}}\right)$$

Modes	θ [°]
1	45
2	45
3	45
4	45
5	45
6	45
7	45
8	45
9	45
10	45

Table 4.3: Wave inclination angle computer

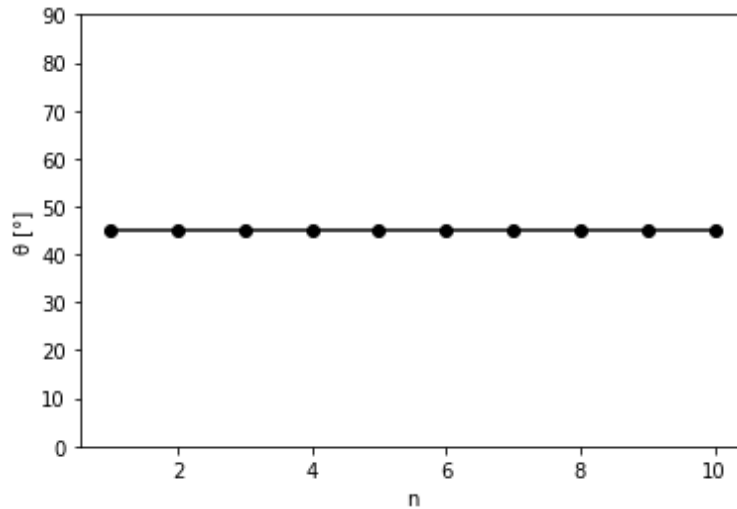


Figure 4.11: Wave inclination angle computed

From Table 4.3, it remarkably appears how reliable is this algorithm: it gives us an accurate and exact value of 45° for all the modes analyzed. The same results are reported in Figure 4.11, where n is the mode number, and will be very important later in the discussion.

4.2.3 Waveform

At this point, the wave inclination angle suggests to extract a line along the identified 45° inclined propagation path to find the waveform of the modes.

In the following figures we report: on top, the extraction line highlighted with the associated color within the crop; on the bottom, the waveform.

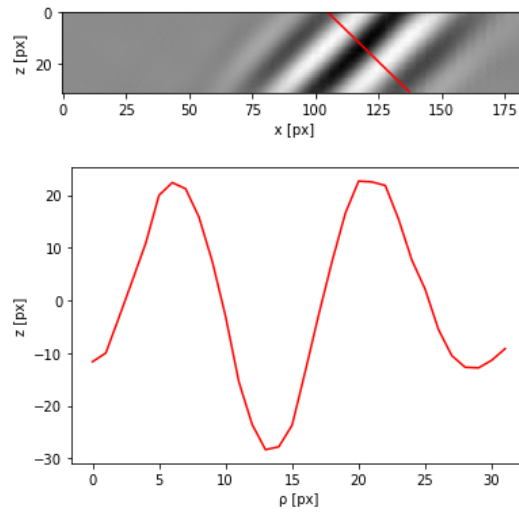


Figure 4.12: Waveform modes 1,2 POD

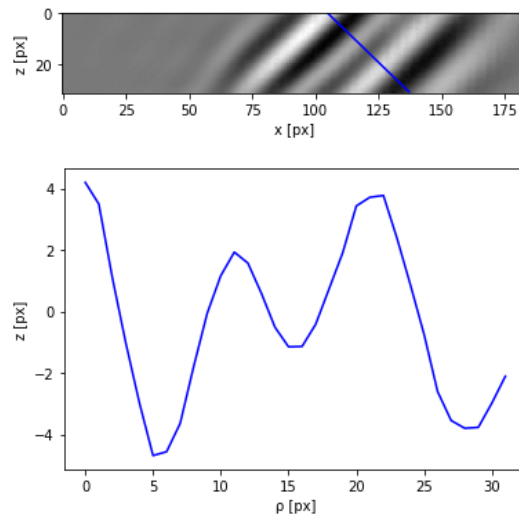


Figure 4.13: Waveform modes 3,4 POD

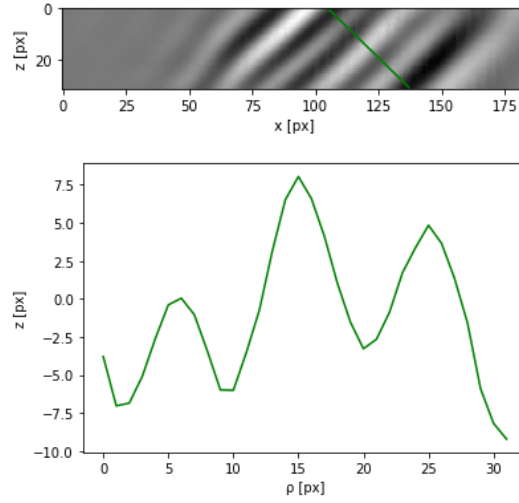


Figure 4.14: Waveform modes 5,6 POD

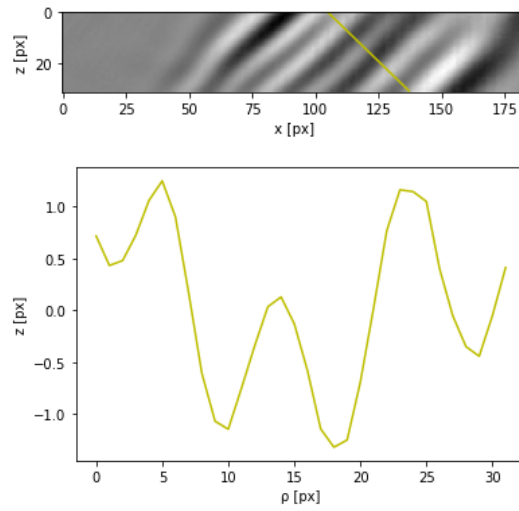


Figure 4.15: Waveform modes 7,8 POD

We arbitrarily selected as starting position for the extraction line the pixel number 105 along the crop bound at a radial coordinate $r/D = 0,9$.

We discuss now the results presented in Figure 4.12 - Figure 4.16:

- Waveform POD modes 1,2 (Figure 4.12):

It appears quite harmonic and quite regular. As we will discuss later on, this is the only waveform that we can extract through POD thanks to its frequency spectra which present a single peak.

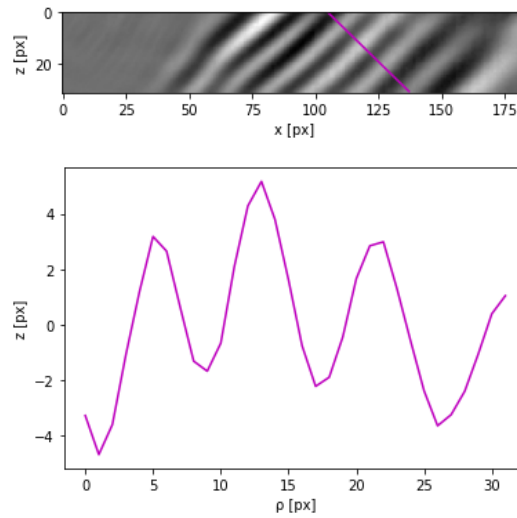


Figure 4.16: Waveform modes 9,10 POD

- Waveform POD modes 3,4 (Figure 4.13):
Some noise appears and there is not an easily recognizable shape. It can be seen as the overlap of two harmonics associated with the two different peaks which characterized its frequency spectra.
- Waveform POD modes 5,6 (Figure 4.14):
Some noise appears and there is not an easily recognizable shape. It can be seen as the overlap of three harmonics associated with the three different peaks which characterized its frequency spectra.
- Waveform POD modes 7,8 (Figure 4.15):
Some noise appears and there is not an easily recognizable shape. It can be seen as the overlap of four harmonics associated with the four different peaks which characterized its frequency spectra.
- Waveform POD modes 9,10 (Figure 4.16):
Some noise appears and there is not an easily recognizable shape. It can be seen as the overlap of five harmonics associated with the five different peaks which characterized its frequency spectra.

Summarizing, spectral mixing prevents us to obtain a recognizable shape from POD modes, with the only exception of the first couple that presents a single frequency peak.

This issue suggests to adopt a different kind of Data-Driven Modal Analysis which allows us to maintain the energy optimality typical of energy-based decomposition and to add the spectral separation typical of frequency-based decomposition. This hybrid method is multi-scale Proper Orthogonal Decomposition and we will discuss later on.

4.2.4 Wave traveling speed

A very interesting property of a wave is its traveling speed. Contrarily to the inclination angle, the speed cannot be directly obtained even from a scrupulous observation of the spatial structures, so we have to adopt a different strategy.

The mathematical tool that we choose to compute the wave traveling speed is Auto-correlation, presented in Appendix B.

Summarizing, once the spatial delay between all the frames has been computed, we can find the traveling speed of each pair of modes by simply dividing it by the duration, defined as the inverse of the sampling frequency.

$$v = \frac{\Delta}{dt}$$

Modes	Speed [m/s]
1,2	332
3,4	338
5,6	340
7,8	338
9,10	340

Table 4.4: Wave traveling speed computed

From Table 4.4, which contains the values computed for the first 10 modes, we can see that we obtain a good approximation of a known value: the speed of sound. The same results are reported in Figure 4.17, where n is the mode number, and will be very important later in the discussion.

The relative errors ϵ between speeds computed and $a \approx 343m/s$, are computed as:

$$\epsilon[\%] = \frac{\|a - v\|}{a} \cdot 100$$

These values are summarized in Table 4.5: for all the pairs of modes analyzed the relative error is approximately 1% or less, except for the first pair of modes where the relative error has a however an acceptable value around 3%.

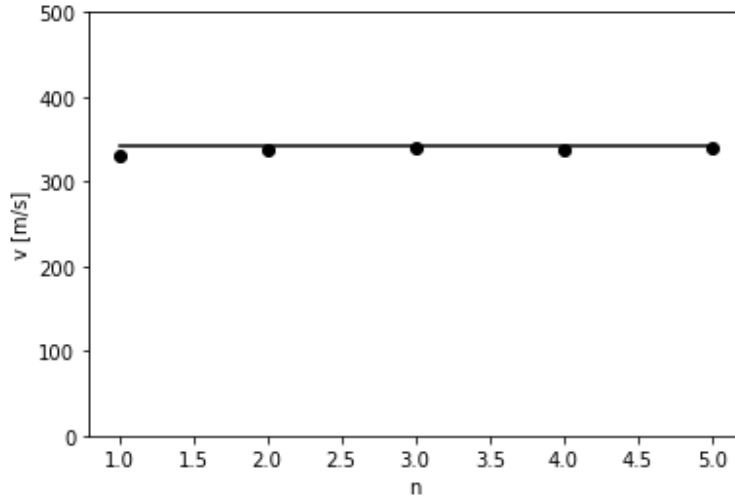


Figure 4.17: Wave traveling speed computed

Modes	Relative error ϵ [%]
1,2	3
3,4	1
5,6	0,5
7,8	1
9,10	0,5

Table 4.5: Wave traveling speed error percentage

4.2.5 Wavelength

After computing the traveling speed of the waves, it becomes immediate to derive the wavelength λ as the ratio between the speed and every single peak within the frequency spectra:

$$\lambda = \frac{v}{f}$$

In Table 4.6 we recap all the wavelengths: their order of magnitude is the centimeter.

The brief analysis carried out in this section proves, once more, how the first coupled modes can be seen as the evolution pattern of a single wave, while the second coupled modes can be seen as the overlap of two waves; the third coupled modes can be seen as the overlap of three waves and so on.

Modes (Peak number)	Frequency peak [kHz]	Wavelength [mm]
1,2 (1)	28	11,8
3,4 (1)	21	16,1
3,4 (2)	37	9,14
5,6 (1)	19	17,9
5,6 (2)	30	11,3
5,6 (3)	41	8,29
7,8 (1)	16	21,1
7,8 (2)	26	13,0
7,8 (3)	35	9,64
7,8 (4)	46	7,34
9,10 (1)	14	24,3
9,10 (2)	23	14,8
9,10 (3)	31	11,0
9,10 (4)	39	8,73
9,10 (5)	51	6,67

Table 4.6: Wavelength

4.2.6 Mach waves

Let us do a brief recap of the main features reached up to now from the coupled modes waves:

- Wave inclination angle: $\theta = 45^\circ$
- Wave travelling speed: $v \approx 343$ m/s

It is well known that waves traveling at the speed of sound along a 45° inclined line are Mach waves [2].

This is the first result that we achieved by applying Data-Driven Modal Analysis to the sound field of a Mach 3 jet: the identification of known structures, in full agreement with achievements obtained from literature [2].

4.2.7 Axial origin coordinate

At this point, it could be interesting to extract the horizontal profiles from the central line of each pair of modes. In the following figures we report: on top, the extraction line highlighted with the associated color within the crop; on the bottom, the horizontal profile.

We discuss now the results presented in Figure 4.18 - Figure 4.22:

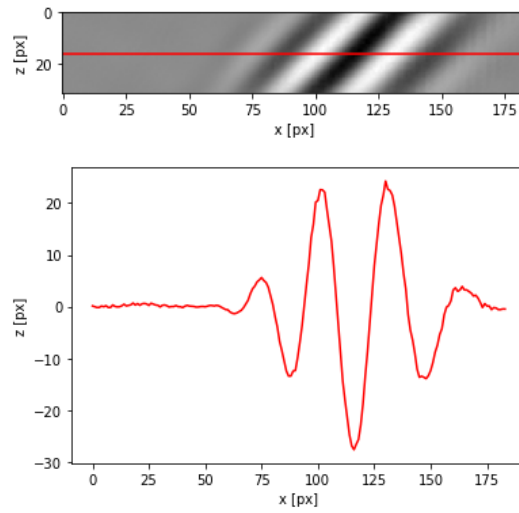


Figure 4.18: Horizontal profile extraction modes 1,2 POD

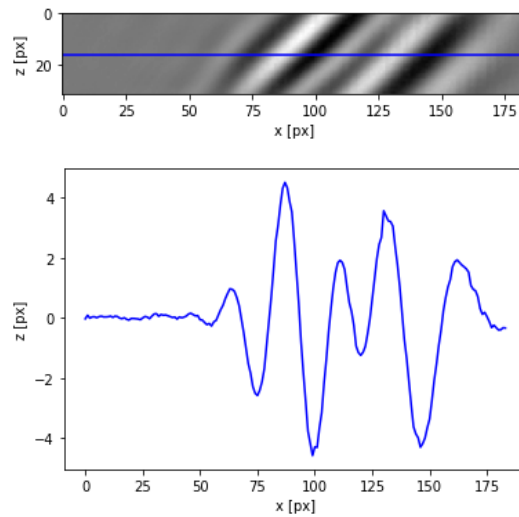


Figure 4.19: Horizontal profile extraction modes 3,4 POD

- Horizontal profile POD modes 1,2 (Figure 4.18):
It looks very regular and symmetric with respect to the larger amplitude oscillation in terms of absolute value. The oscillations start from a certain coordinate after an initial region of a flat signal.
- Horizontal profile POD modes 3,4 - 9,10 (Figure 4.19 - Figure 4.22):
They look not regular at all and we are not able to identify any kind of

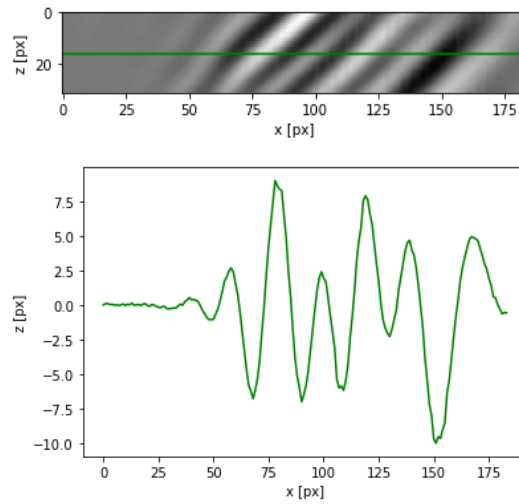


Figure 4.20: Horizontal profile extraction modes 5,6 POD

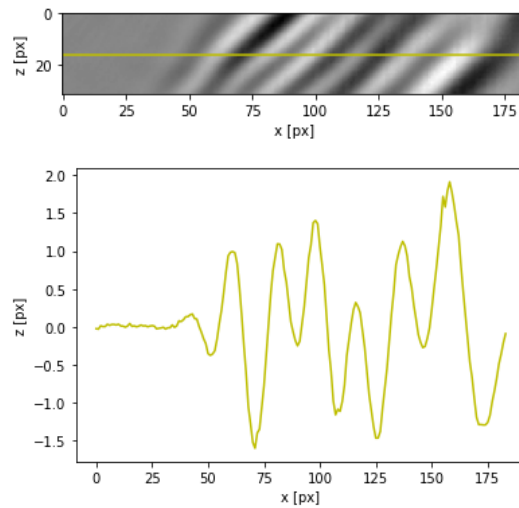


Figure 4.21: Horizontal profile extraction modes 7,8 POD

symmetry. The signals stay flat for shorter portions because a wider range of frequencies is involved.

As we will see in the next section, this lack of regularity and symmetry, within the couples of modes successive to the first one, is due to the plurality of frequency peaks in their frequency spectra.

In Figure 4.23, through modes superposition, we checked the reliability of POD.

- First 10 modes superposition: it shows features much more similar to the

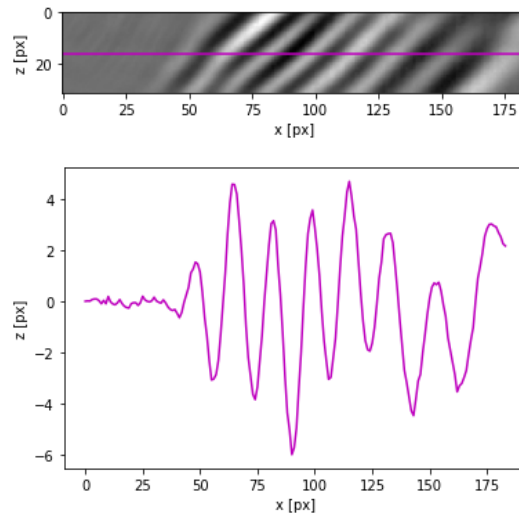


Figure 4.22: Horizontal profile extraction modes 9,10 POD

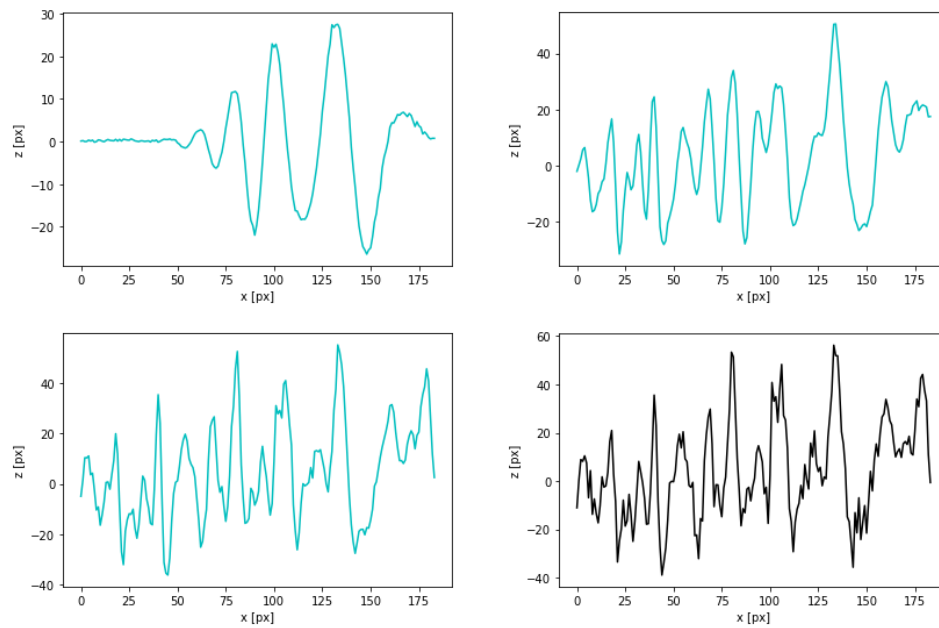


Figure 4.23: POD modes superposition: first 10 modes (top-left), first 100 modes (top-right) and first 1000 modes (bottom-left), original signal (bottom-right)

single coupled modes profile than to the original crop and it emerges at a certain coordinate along the x-axis.

- First 100 modes superposition: it starts to broadly remind the trend of the

original crop with peaks positions that are qualitatively well matched.

- First 1000 modes superposition: it becomes more and more like the original crop and the differences between them become hard to find.

So, thanks to mode superposition, we confirmed the accuracy of POD and we had another demonstration that the modes are sorted according to decreasing energy: the difference between the first 10 modes superposition and the first 100 modes superposition is significantly greater than the difference between the first 100 modes superposition and the first 1000 modes superposition, which in turn is considerably larger than the difference between the first 1000 modes superposition and original crop. By the way, this can be understood from how negligible are the contributes of the modes after mode 1000.

By accurately observing these horizontal profiles it appears how, at some point after a portion of the crop where the signal is almost flat, waves gradually begin to emerge and undergo a considerable amplitude increase. Also from the spatial structures analyzed previously was possible to note this growth, but only through the horizontal profile, we can quantify it.

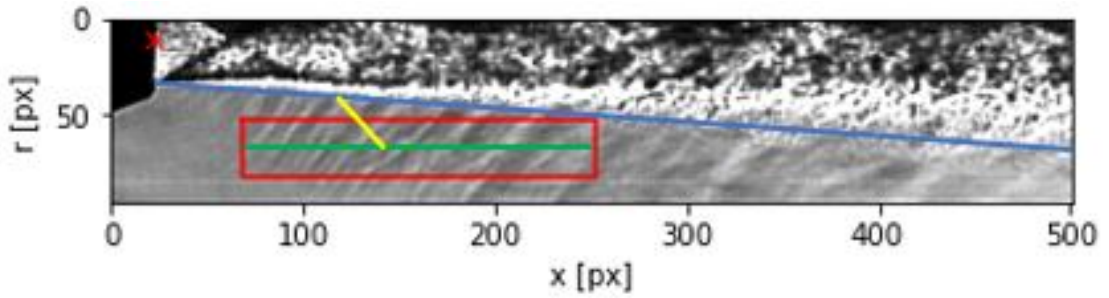


Figure 4.24: x/D origin referred to boundary layer scheme

Starting from this observation we derived the so-called axial origin coordinate, defined as the coordinate along the x -axis from which waves are emitted, by using the known propagation angle of Mach waves. We must remember the physical origin of that waves: they are born from turbulent structures inside the jet shear layer which have a supersonic convective speed.

So the formula which leads to compute axial origin coordinate is:

$$\left(\frac{x}{D}\right)_{origin} = \left(\frac{x}{D}\right)_{amplitude=10\%} - \frac{\left(\frac{r}{D}\right)_{crop,max} + \left(\frac{r}{D}\right)_{crop,min} - 1}{2} + 0,1\left(\frac{x}{D}\right)_{origin}$$

We can compute axial origin coordinate thanks to the formulation above which can be split into three different components with reference to Figure 4.24:

- Threshold coordinate: $\left(\frac{x}{D}\right)_{amplitude=10\%}$

We compute the axial coordinate where the amplitude of the signal exceeds a threshold fixed at 10% of its maximum amplitude: below this value, the detected signal is considered as background noise; above this value, the detected signal is considered as the real wave.

- Crop position correction: $-\frac{\left(\frac{r}{D}\right)_{crop,max} + \left(\frac{r}{D}\right)_{crop,min} - 1}{2}$

At this point we have to get this coordinate back to the jet exit radial coordinate. The propagation angle $\lambda = 45^\circ$ allows us to solve that task by translating, through a subtraction, of a quantity (yellow line in Figure 4.24) equals to the radial coordinate of the crop central horizontal line (green line in Figure 4.24) along the axial coordinate, and by adding $\frac{1}{2}$ because waves born inside shear layer and not along the jet axis.

- Boundary layer correction: $0,1\left(\frac{x}{D}\right)_{origin}$

The last step consists in the sum of the boundary layer thickness (blue line in Figure 4.24) which is known to be $y = 0,1x$. In this case it becomes $\left(\frac{r}{D}\right)_{origin} = 0,1\left(\frac{x}{D}\right)_{origin}$ where the subscript denotes the origin axial coordinate computed after the firsts two steps.

Modes	x/D origin [-]
1,2	2,00
3,4	1,73
5,6	1,41
7,8	1,33
9,10	1,25

Table 4.7: x/D origin

In summary, the analyzed waves originate inside the jet shear layer from an axial coordinate between 1,25 and 2 jet diameters; it decreases when the frequency spectra involve higher frequencies. The same results are reported in Table 4.11 and in Figure 4.25, where n is the mode number.

4.2.8 Skewness statistical indicator

A method that allows us to obtain an insight about steepening is skewness analysis, a statistical indicator presented in Appendix C, which gives a measure of the asymmetry of a signal.

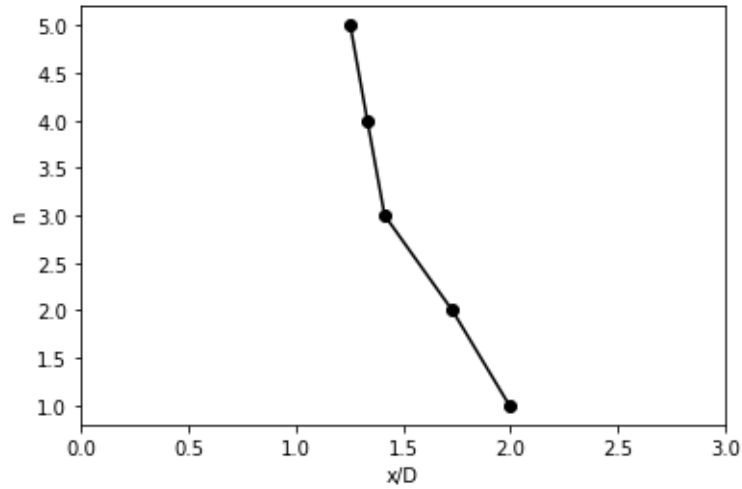


Figure 4.25: x/D origin coordinate

Modes	Skewness statistical indicator
1,2	-0,026
3,4	0,045
5,6	-0,011
7,8	-0,013
9,10	-0,004
First 100 sum	0,23
First 1000 sum	0,38
Complete	0,36

Table 4.8: Skewness value

Table 4.8 recaps some relevant skewness values:

- The first five pairs of modes deeply analyzed so far have very small skewness values. This suggests that steepening is not detected within them.
- Mode 100 is a halfway mode. The reconstruction of the first 100 modes has a skewness value slightly larger than half of the complete reconstruction one.
- Mode 1000 is a boundary mode. The reconstruction of the first 1000 modes has a skewness value almost equal to the complete reconstruction one.
- Complete reconstruction shows a skewness value which is little in absolute terms, but quite different from the values of the first modes, so we have to identify which modes are responsible for this difference.

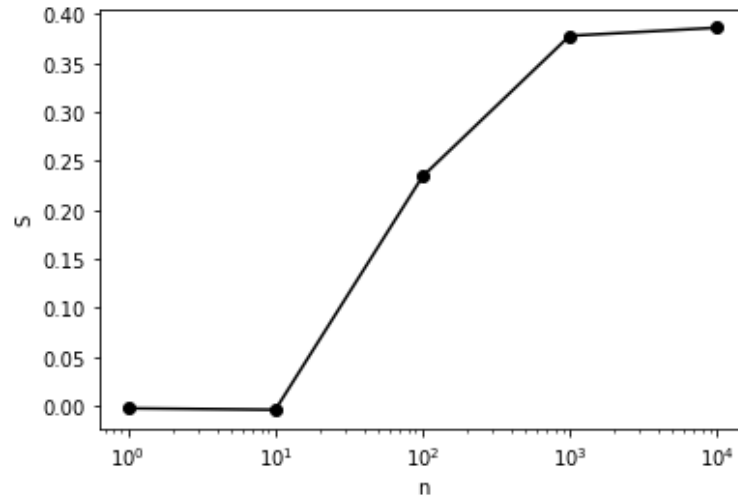


Figure 4.26: Skewness trend

Figure 4.26 graphically shows how the steepening is almost completely included between mode 10 and mode 1000. Note that the x-axis follows a logarithmic scale and so, also if the slope is similar, more than half of the total steepening is contained within only 90 modes (between mode 11 and mode 100), while the remaining steepening is distributed among 900 modes (between mode 101 and mode 1000).

In summary, the signal slightly goes towards a saw-tooth-like structure, characterized by sharp compressions followed by gradual expansions, but this process is detected in a quantity which is not large enough to induce crackle noise.

4.3 Multi-scale Proper Orthogonal Decomposition (mPOD)

The multi-scale Proper Orthogonal Decomposition technique, presented in the previous chapter, brings us to 3700 modes, a significantly lower number compared to POD one, due to spectral separation. Also, mPOD sort modes so that the first mode is the most energetic one and the last mode is the least energetic one.

To properly implement mPOD, we have to compute the frequency spectrum of the temporal correlation matrix \widehat{K} , see Figure 4.27. The computed matrix is symmetric and its anti-diagonal contains the information we are searching for. Unfortunately, along this diagonal is not clear what are the dominant frequencies, so we have to develop a trick that allows us to find them.

Going back to POD results we consider the frequency spectra of the coupled

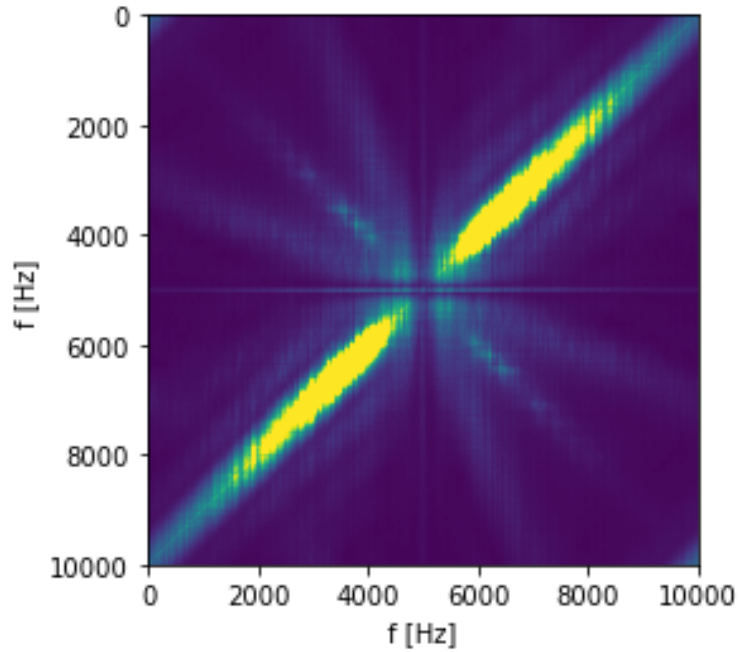


Figure 4.27: Frequency spectrum temporal correlation matrix

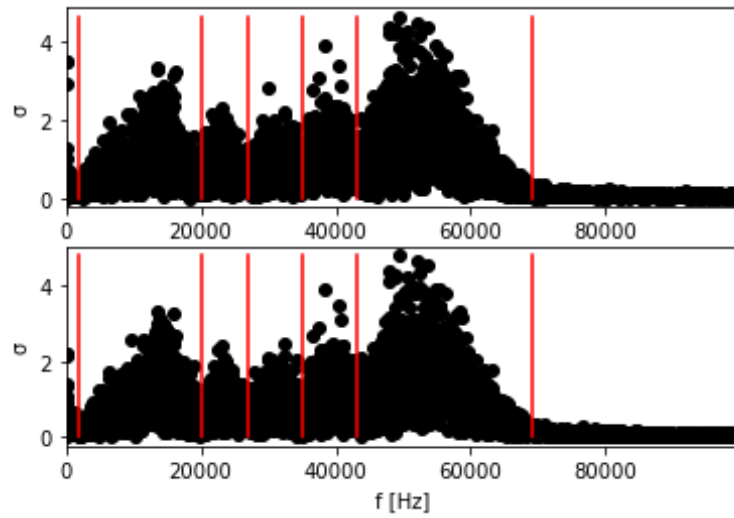


Figure 4.28: Frequency splitting vector from POD modes 9,10

modes: we found how the first pair of modes has a single frequency peak, the second pair of modes has two frequency peaks, the third pair of modes has three frequency peaks and so on. So we assumed that peaks to be the ones hidden into the matrix anti-diagonal: among all the tested combinations we noticed that the

one which allows us to better grasp spectral separation is the fifth pair of POD modes, composed by mode 9 and mode 10. These frequency peaks suggest to use the frequency splitting vector obtained from Figure 4.28 and summarized in Table 4.9.

Filter	Frequency range [Hz]
Low-pass	$f < 2000$
Band-pass 1	$2000 < f \leq 20000$
Band-pass 2	$20000 < f \leq 27000$
Band-pass 3	$27000 < f \leq 35000$
Band-pass 4	$35000 < f \leq 43000$
Band-pass 5	$43000 < f \leq 69000$
High-pass	$f \geq 69000$

Table 4.9: mPOD transfer function filters from POD modes 9,10

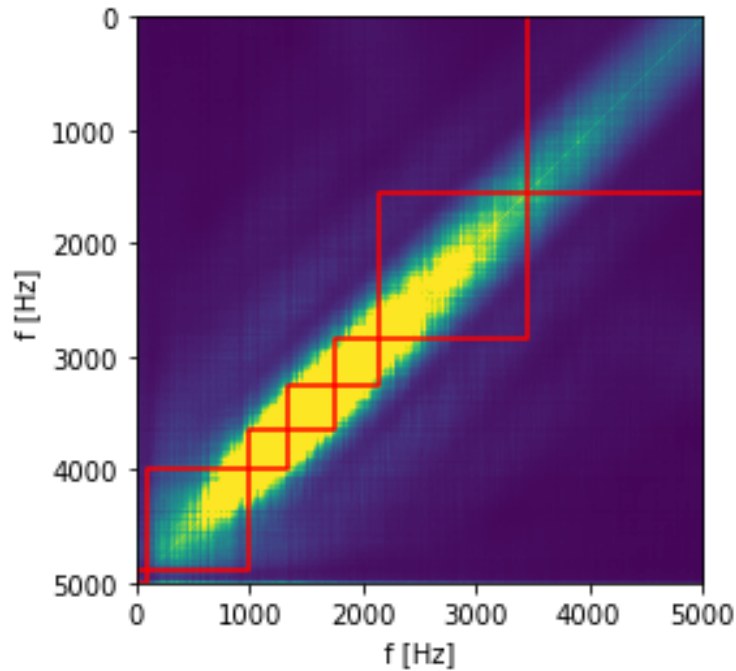


Figure 4.29: \widehat{K} frequency splitting vector from POD modes 9,10

This matrix partition also allows us to neglect all the contributes outside the red squares in Figure 4.29 thanks to mPOD properties: this explains why the number of modes resulting from this decomposition is lower than the one previously obtained from POD, which instead considered the complete matrices. Note that

here it is shown only an orthant that contains the anti-diagonal and the red squares were built by matching the chosen frequency splitting vector.

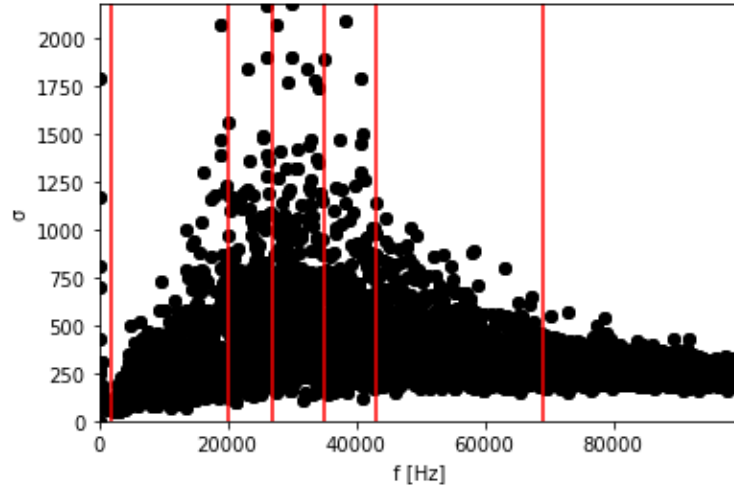


Figure 4.30: \widehat{K} diagonal frequency splitting vector from POD modes 9,10

The last step is to extract the aforementioned diagonal, which contains the required information. The results of this overlap are shown in Figure 4.30.

Now, we are ready to go into the heart of the mPOD discussion: it will allow us to find modes cleaned from any kind of spectral mixing.

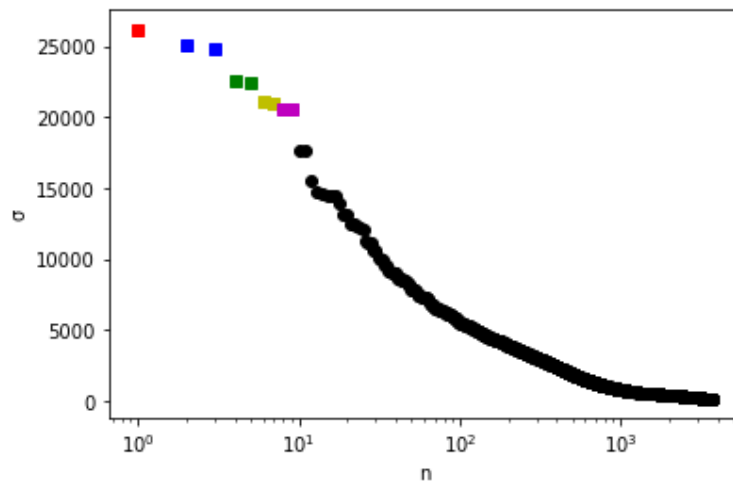


Figure 4.31: σ decay mPOD

A first way to visualize the results of this decomposition is to plot the σ decay as in Figure 4.31. This plot shows the amplitudes of every single mode along the

y-axis and the number of the modes along the x-axis. The x-axis is represented in a logarithmic scale to focus the attention on the more energetic modes.

It is worth noting that POD modes are coupled: first with second, third with fourth, fifth with sixth, and so on. Deeply observing:

- σ of the modes which compose a pair is similar;
- σ of the modes within a couple is well distinct from that of nearby couples;
- increasing mode number σ get closer.

During this analysis, we will use a convention to focus on the first 10 modes, highlighted in Table 4.10, which recap the composition of every couple of modes and associate them a color.

Pair	Modes	Color
1	1,2	Red
2	3,4	Blue
3	5,6	Green
4	7,8	Yellow
5	9,10	Magenta

Table 4.10: Convention mPOD

4.3.1 Spatial structures and frequency spectra

Following the steps of what we have done for POD, we start mPOD discussion from the spatial structures and the frequency spectra.

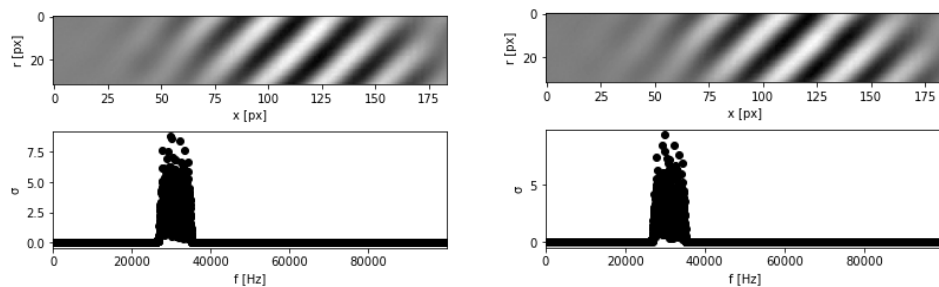


Figure 4.32: mPOD modes 1,2: spatial structures and frequency spectra

Spatial structures correspond to the matrix Φ (see chapter 3), reshaped from column arrays into $n_x \times n_y$ matrices. Frequency spectra represent σ amplitudes

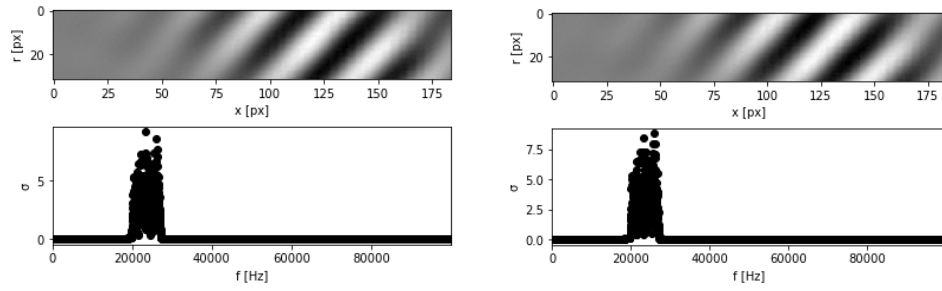


Figure 4.33: mPOD modes 3,4: spatial structures and frequency spectra

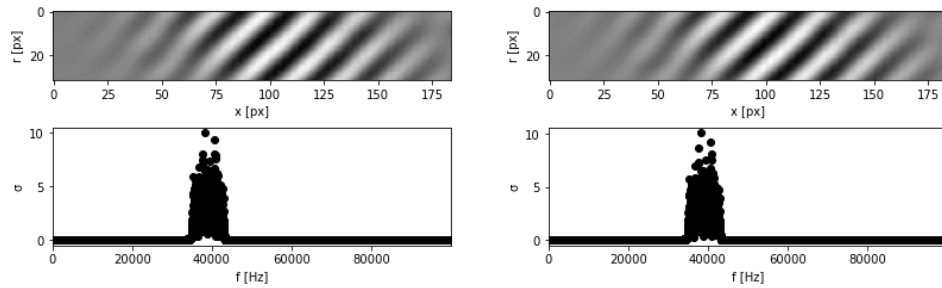


Figure 4.34: mPOD modes 5,6: spatial structures and frequency spectra

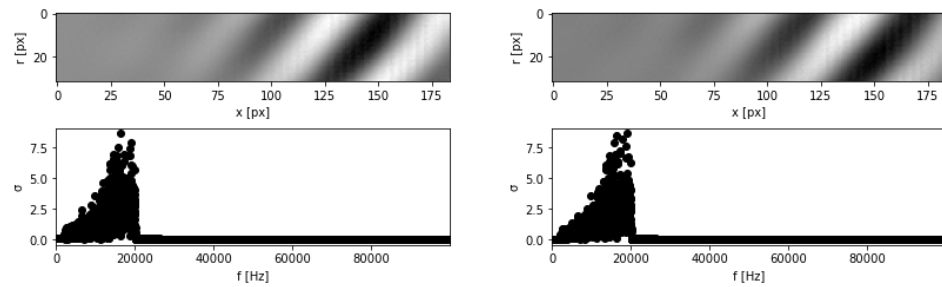


Figure 4.35: mPOD modes 7,8: spatial structures and frequency spectra

associated with frequencies. Bearing in mind that we want to highlight the relationship between the two modes which form a pair, we can make some observations in detail case by case:

- mPOD modes 1,2 (Figure 4.32):
 Spatial structures reveal wave insurgency from a certain coordinate, they appear as very regular and they show a certain inclination.
 Frequency spectra are characterized by a single peak at a value ranging from 27 kHz to 35 kHz.

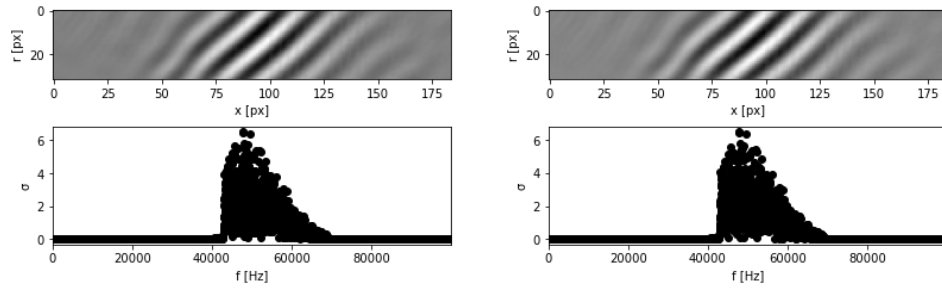


Figure 4.36: mPOD modes 9,10: spatial structures and frequency spectra

- mPOD modes 3,4 (Figure 4.33):

Spatial structures reveal wave insurgency from a certain coordinate, they appear as very regular and presents fewer oscillations than the first pair, due to a lower frequency range as we will see, and they show a certain inclination.

Frequency spectra are characterized by a single peak at a value ranging from 20 kHz to 27 kHz.

- mPOD modes 5,6 (Figure 4.34):

Spatial structures reveal wave insurgency from a certain coordinate, they appear as very regular and presents more oscillations than the previous pairs, due to a higher frequency range as we will see, and they show a certain inclination.

Frequency spectra are characterized by a single peak at a value ranging from 35 kHz to 43 kHz.

- mPOD modes 7,8 (Figure 4.35):

Spatial structures reveal wave insurgency from a certain coordinate, they appear as very regular and presents fewer oscillations than the previous pairs, due to a lower frequency range as we will see, and they show a certain inclination.

Frequency spectra are characterized by a single peak at a value ranging from 2 kHz to 20 kHz.

- mPOD modes 9,10 (Figure 4.36):

Spatial structures reveal wave insurgency from a certain coordinate, they appear as very regular and presents more oscillations than the previous pairs, due to a higher frequency range as we will see, and they show a certain inclination.

Frequency spectra are characterized by a single peak at a value ranging from 43 kHz to 69 kHz.

We can see how spatial structures are coupled and complementary like in POD, but applying mPOD spectral separation produces a very regular pattern.

So mPOD frequency spectra differ significantly from the POD case by isolating every single frequency band, and this allows us to understand the following mechanism: phenomena characterized by higher frequency require less space to evolve than lower frequency involving ones. We can conclude that what we considered the axial origin coordinates of the higher frequencies cases are nearest to the jet exit than the axial origin coordinates of the lower frequencies cases.

4.3.2 Waveform

Thanks to its spectral separation mPOD allows us to separate every single frequency peak associated waveform, while in POD waveform spectral mixing generates an overlap which affects all the pairs of modes except the first ones, where frequency spectra had only a single peak.

We summarize the extraction line starting position as pixel numbers along the crop bound, selected for the different pairs of modes, at a radial coordinate equals to $r/D = 0,9$ in Table 4.11.

In the following figures we report: on top, the extraction line highlighted with the associated color within the crop; on the bottom, the waveform.

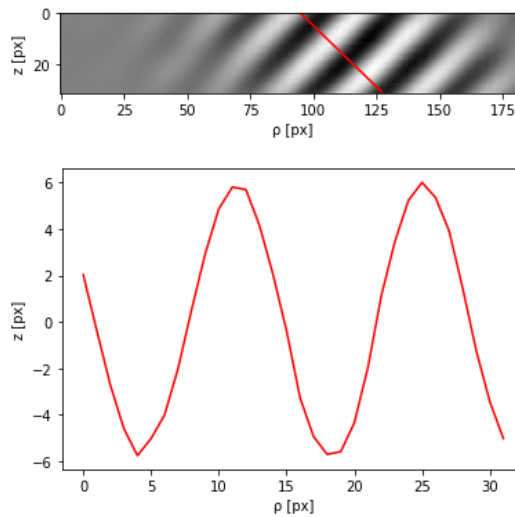


Figure 4.37: Waveform modes 1,2 mPOD

We discuss now the results presented in Figure 4.12 - Figure 4.16:

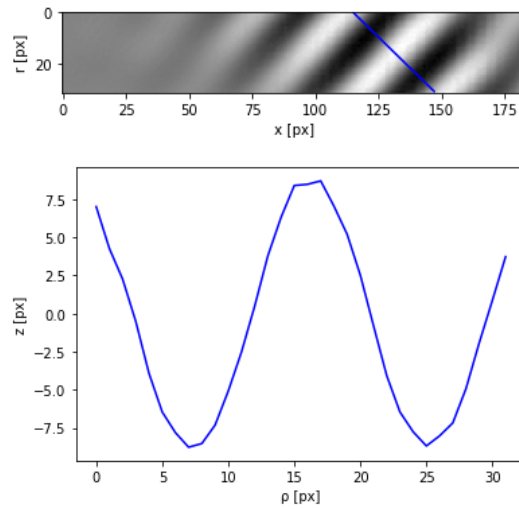


Figure 4.38: Waveform modes 3,4 mPOD

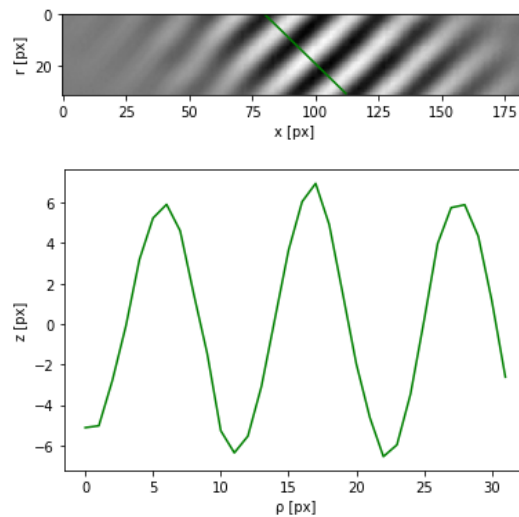


Figure 4.39: Waveform modes 5,6 mPOD

- Waveform mPOD modes 1,2 (Figure 4.37):
It is harmonic, regular, and it does not differ too much from the corresponding waveform extracted from POD. As already mentioned, the reason for this similarity is probably due to the single peak shape of POD modes 1,2, but this is an exception as we are going to see next.
- Waveform mPOD modes 3,4 (Figure 4.38):

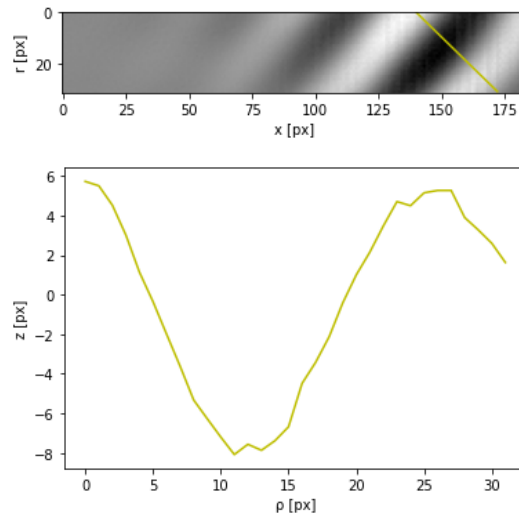


Figure 4.40: Waveform modes 7,8 mPOD

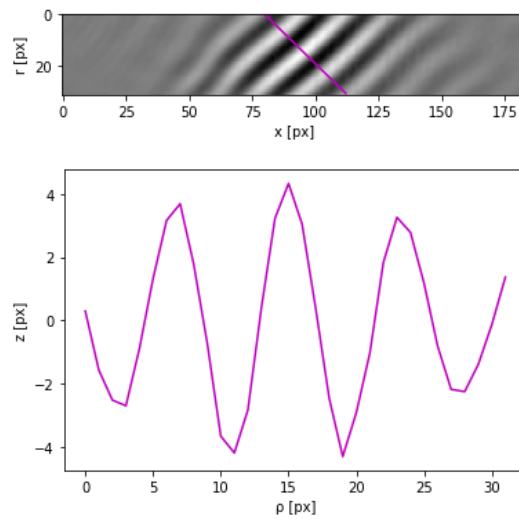


Figure 4.41: Waveform modes 9,10 mPOD

It is harmonic, regular, completely different from the corresponding waveform extracted from POD, which could be seen as the overlap of two harmonic. This waveform has fewer oscillations than the first pair due to a lower frequency range.

- Waveform mPOD modes 5,6 (Figure 4.39):

It is harmonic, regular, completely different from the corresponding waveform

extracted from POD, which could be seen as the overlap of three harmonic. This waveform has more oscillations than the previous pairs due to a higher frequency range.

- Waveform mPOD modes 7,8 (Figure 4.40):

It is harmonic, regular, completely different from the corresponding waveform extracted from POD, which could be seen as the overlap of four harmonic. This waveform has fewer oscillations than the previous pair due to a lower frequency range.

- Waveform mPOD modes 9,10 (Figure 4.41):

It is harmonic, regular, completely different from the corresponding waveform extracted from POD, which could be seen as the overlap of five harmonic. This waveform has more oscillations than the previous pairs due to a higher frequency range.

In conclusion, mPOD allows us to properly extract waveforms and shows how their shapes are undoubtedly harmonic. Another way of looking at this finding is that the dataset pairs harmonics in space with harmonics in time.

Modes	Extraction line starting position [px]
1,2	95
1,2	115
1,2	80
1,2	140
1,2	80

Table 4.11: Extraction line starting position

Two last remarks confirm some results we already found during the discussion:

- Structures which involve higher frequencies require less space to fully develop, by arising and by reaching their maximum at lower coordinates, compared to ones characterized by lower frequencies.
- Structures which involve higher frequencies origin closer to the jet exit: what we defined as axial origin coordinate is lower and so they appear earlier within the crop, compared to ones characterized by lower frequencies. Therefore we selected lower values of extraction line starting position for higher frequencies modes, and higher values of extraction line starting position for lower frequencies modes in Table 4.11.

Chapter 5

Conclusions

5.1 Recap of main results

Let us now briefly summarize the main results of the presented analysis.

Both POD modes and mPOD modes derived by Modal Analysis reveal to be coupled. In these decompositions, the modes are sorted from the more energetic to the less energetic ones, and they are organized in couples. By rebuilding every single pair at a time we found propagating wave patterns.

Observing in detail the POD case, we cataloged the discovered modes as Mach waves mainly thanks to the following features:

- The propagation angle equals 45° . According to literature [2], Mach waves have a very high directivity which allows them to propagate only along a 45° inclined path: thanks to 2-D FFT (Appendix A) we checked that the waves respect this criterion.
- The traveling speed is approximately the speed of sound. From the definition of Mach waves, we know how they have to propagate at the speed of sound. By using auto-correlation (Appendix B) the errors between the theoretical values and the computed values are negligible: around 1%, with the only exception of the first pair of modes whose error is still acceptable, around 3%.

Thanks to skewness statistical indicator we were able to detect wave steepening. The first 10 modes which we analyzed in detail are not involved in any kind of non-linearities, but the use of that particular statistic indicator reveals a slight steepening hidden between mode 11 and mode 1000.

Focusing on mPOD we isolated the waveforms of every single couple of modes by extracting oblique lines along the propagation path. Their spatial structures showed purely harmonic characteristics revealing that, within the hydrodynamic

field and the near-acoustic field of the supersonic jet, any kind of steepening was not detected. So we can conclude that the data accurately pairs harmonics in space with harmonics in time.

5.2 Open questions

The results summarized in the above section leave some open questions that deserve to be analyzed more in detail. This study revealed that the waveform of the more energetic modes within the hydrodynamic field and acoustic near-field are harmonic and any kind of steepening has not been detected. Indeed, though skewness statistical indicator, non-linearities have been slightly discovered between mode 20 and mode 200.

Despite this, it would be interesting to repeat this analysis in a wider region by applying Data-Driven Modal Analysis also going towards the acoustic far-field. In this way, we can understand if more energetic modes waveforms stay linear along their complete propagation path or if the narrowness of the observation area, which depends on the original schlieren dataset, prevents us from detecting nonlinearities. Also within the modes involved by a light steepening, it would be interesting to understand if they may steepen more across a wider observation area.

From the previous study, we know that non-linearities may lead Mach waves to saw-tooth-like structures which rise crackle noise. Since the latter is the most annoying component of the whole acoustic sound field, an interesting target may be to discover if somehow is possible to preserve linearity, or at least to limit the potential non-linear effects: to keep the waveforms as regular as possible should bring supersonic jet noise emissions to a more gentle increase.

Appendix A

2-D Fast Fourier Transform

Fast Fourier Transform (FFT) is an algorithm which implement the Discrete Fourier Transform (DFT) of a signal. Its bi-dimensional version is computed by simply multiplying the FFT along a direction x and the FFT along another direction y as in the formula below:

$$FFT[k_x, k_y] = \frac{1}{N_x N_y} \sum_{m=0}^{N_x-1} \sum_{l=0}^{N_y-1} \Phi[m, l] e^{-j2\pi \left(\frac{k_x m}{N_x} + \frac{k_y l}{N_y} \right)}$$

This expression has a length of N_x values along the x-axis and N_y values along the y-axis and gives as result a periodic and sampled transform starting from a periodized signal. The 2-D FFT is a function of the wavenumbers k_x and k_y and the values that they assume where the function reaches its peak allow us to compute pattern directivity.

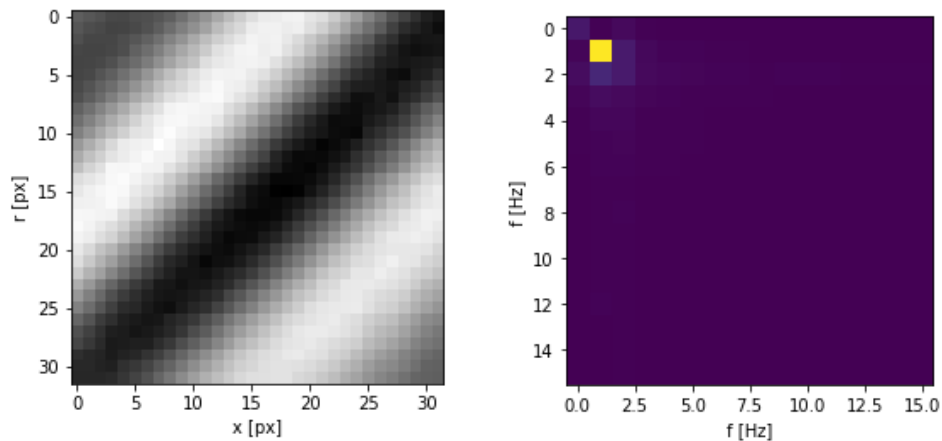


Figure A.1: 2-D FFT spatial structure and frequency spectrum

Figure A.1 shows: on the left the narrow area where we shrink the crop to obtain more solid results from this analysis; on the right the frequency spectrum given by 2-D FFT.

Once we computed wavenumbers along the involved axes corresponding to the peak of the 2-D FFT, wave propagation angle is the arctangent of the ratio between them. As we can expect in this particular case the computed wavenumbers are equal to each other, so wave propagation angle will have a value of $\theta = 45^\circ$.

Appendix B

Auto-correlation

Cross-correlation in Signal Processing detect the similarity between two signals where a displacement, which can be spatial or temporal, has been applied to one of them. The auto-correlation, whose definition is indicated below, can be seen as a cross-correlation of the same function in following instant:

$$\rho_{\Phi_i, \Phi_{i+1}}(\tau) = \int_{-\infty}^{+\infty} \overline{\Phi_i(t)} \Phi_{i+1}(t + \tau) d\tau$$

This relation is a function of τ and allows us to define the delay, either spatial or temporal, between a signal Φ_i and another signal Φ_{i+1} . However, the lag corresponds to the peak of the auto-correlation function and it should be almost constant among all frames.

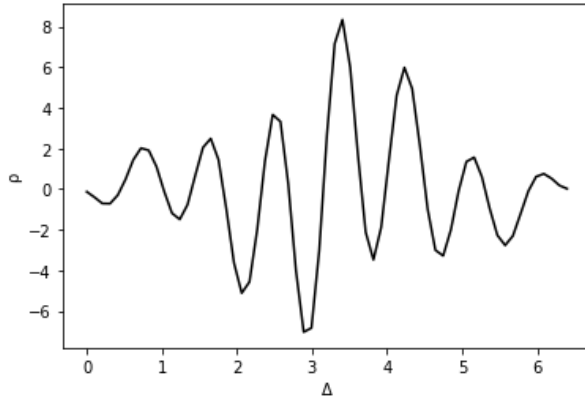


Figure B.1: Auto-correlation

In Figure B.1 we can see the auto-correlation between two following frames. The peak of the function is reached at a value that is almost constant scrolling

through all the frames contained in the dataset and this proves the robustness of the algorithm.

For this analysis the auto-correlation focus is on the spatial displacement case, then we will easily compute wave propagation speed by dividing for the time lag between two following frames, a quantity which is defined as the inverse of the sampling frequency that is known from the dataset. As expected, the computed wave traveling speed is around the speed of sound $a \approx 343m/s$.

Appendix C

Skewness

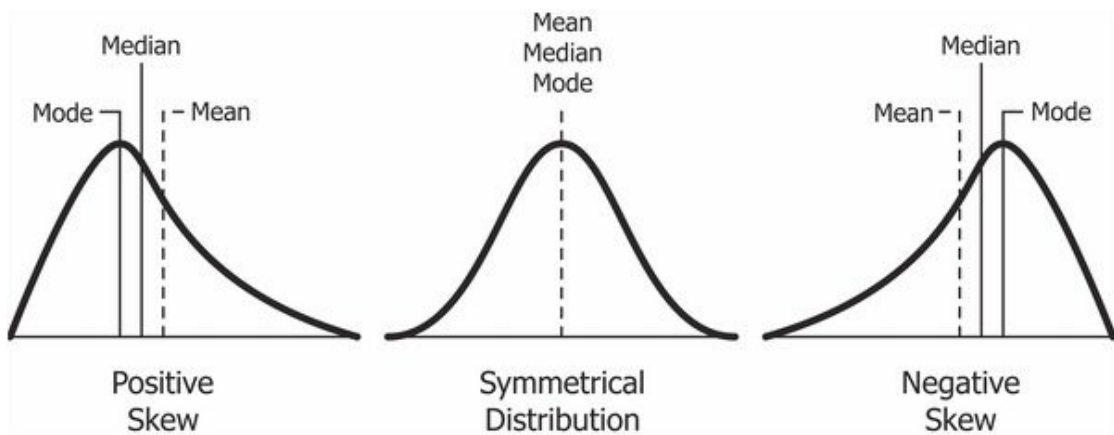


Figure C.1: Skewness working

Skewness is a statistical indicator which gives a measure of the asymmetry of a signal ϕ_i defined as below, where σ is standard deviation:

$$S = \frac{\sum_{i=1}^{n_t} (\phi_i - \bar{\phi})^3}{n_t \sigma^3}$$

In Figure C.1 we have a recap of qualitative indication given by of this statistical indicator and applying it to the signal is clear how:

- if $S > 0$: the signal is characterized by sharp compressions followed by gradual expansions.
- if $S = 0$: compressions and expansions have the same mean slope along the signal.

- if $S < 0$: the signal is characterized by gradual compressions followed by sharp expansions.

As far as quantitative information is concerned, we can say that:

- if $-0,5 < S < 0,5$: data are nearly symmetrical
- if $-1 < S < -0,5$ or $0,5 < S < 1$: data are moderately skewed
- if $S < -1$ or $S > 1$: data are highly skewed

Bibliography

- [1] Charles E. Tinney and Woutijn J. Baars. *Supersonic jet noise phenomena and crackle* (cit. on p. 2).
- [2] Woutijn J. Baars and Charles E. Tinney. «Shock-structures in the acoustic field of a Mach 3 jet with crackle». In: *Journal of Sound and Vibration* (2014) (cit. on pp. 3, 32, 50).
- [3] W. J. Baars C. E. Tinney M. S. Wochner and M. F. Hamilton. «On cumulative non-linear acoustic waveform distortions from high-speed jets». In: *J. Fluid Mech.* vol. 749 (2014), pp. 331–366 (cit. on p. 4).
- [4] Romain Fievet Charles E. Tinney Woutijn J. Baars and Mark F. Hamilton. «Coalescence in the sound field of a laboratory-scale supersonic jet». In: *AIAA Journal* (2016) (cit. on p. 4).
- [5] Pierre Pineau and Christophe Bogey. «Study of the generation of shocks by high-speed jets using conditional averaging». In: *AIAA Aviation forum* (2018) (cit. on p. 4).
- [6] Pierre Pineau and Christophe Bogey. «Steepened Mach waves near supersonic jets: study of azimuthal structure and generation process using conditional averages». In: *J. Fluid Mech.* vol. 880 (2019), pp. 594–619 (cit. on p. 4).
- [7] Charles E. Tinney and Christophe Schram. «Acoustic modes from a Mach 3 jet». In: *Aeroacoustics Conferences* (2019) (cit. on p. 4).
- [8] Charles E. Tinney and John Valdez. *Overview of Mach 3 Nozzle Databases*. Applied Research Laboratories, The University of Texas at Austin, 10000 Burnet Rd. Austin, TX 78758 (cit. on p. 6).
- [9] G. Strang. *Computational Science and Engineering*, pp. 70–76 (cit. on p. 12).
- [10] P. Holmes J. L. Lumley G. Berkooz and C. Rowley. «Turbulence, Coherent Structures, Dynamical Systems and Symmetry». In: *2nd edn. Cambridge University Press* (2012) (cit. on p. 15).
- [11] P. Holmes J. L. Lumley G. Berkooz J. C. Mattingly and R. W. Wittenberg. «Low-dimensional models of coherent structures in turbulence». In: *Phys. Rep.* 287 (4) (1999), pp. 337–384 (cit. on p. 15).

- [12] L. Sirovich. «Turbulence and the dynamics of coherent structures: Part i. coherent structures». In: *Quart. Appl. Math* 45 (3) (1987), pp. 561–571 (cit. on p. 15).
- [13] L. Sirovich. «Chaotic dynamics of coherent structures». In: *Physica D* 37 (1) (1989), pp. 126–145 (cit. on p. 15).
- [14] L. Sirovich. «Analysis of turbulent flows by means of the empirical eigenfunctions». In: *Fluid Dyn. Res.* 8, 85-100 (1991), pp. 85–100 (cit. on p. 15).
- [15] J. L. Lumley. «The structures of inhomogeneous turbulent flows». In: *Atmospheric turbulence and radio propagation* (ed. A. M. Yaglom, V. I. Tatarski (1967), pp. 166–178 (cit. on p. 15).
- [16] J. L. Lumley. «Stochastic Tools in Turbulence». In: *DOVER PUBN INC* (1970) (cit. on p. 15).
- [17] G. Berkooz J. Elezgaray P. Holmes J. Lumley and A. Poje. «The proper orthogonal decomposition, wavelets and modal approaches to the dynamics of coherent structures». In: *Appl. Sci. Res.* 53 (3-4) (1994), pp. 321–338 (cit. on p. 15).
- [18] G. Berkooz P. Holmes J. L. Lumley. «The proper orthogonal decomposition in the analysis of turbulent flows». In: *Annu. Rev. Fluid Mech.* (1993), pp. 539–575 (cit. on p. 15).
- [19] M. A. Mendez M. Balabane J.-M. Buchlin. «Multi-Scale Proper Orthogonal Decomposition of Complex Fluid Flows». In: *arXiv.org > physics > arXiv:1804.09646* (2019) (cit. on p. 18).
- [20] Miguel A Mendez David Hess Bo B Watz Jean-Marie Buchlin. «Multi-scale Proper Orthogonal Decomposition (mPOD) of TR-PIV data– a Case Study on stationary and Transient Cylinder Wake Flows». In: *arXiv.org > physics > arXiv:2001.01971* (2020) (cit. on p. 18).
- [21] Davide Ninni Miguel A Mendez. «MODULO: A software for Multiscale Proper Orthogonal Decomposition of data». In: *arXiv.org > physics > arXiv:2004.12123* (2020) (cit. on p. 18).